Observed diurnal cycles of near-surface shear and stratification in the equatorial Atlantic and their wind dependence

A. C. Hans[1], P. Brandt[1,2], F. Gasparin[3], M. Claus[1,2], S. Cravatte[3,4], J. Horstmann[5] and G. Reverdin[6]

[1] GEOMAR Helmholtz Centre for Ocean Research Kiel, Kiel, Germany [2] Faculty of Mathematics and Natural Sciences, Kiel University, Kiel, Germany [3] Université de Toulouse, LEGOS (IRD/UT3/CNES/CNRS), Toulouse, France [4] IRD Center, Nouméa, New Caledonia [5] Helmholtz Centre Hereon, Radar Hydrography, Geesthacht, Germany [6] Sorbonne Université - CNRS - IRD - MNHN, Laboratoire LOCEAN - IPSL, Paris, France

Corresponding author: Anna Christina Hans (ahans@geomar.de)

Key Points:

- In the upper 15 m of the equatorial Atlantic Ocean, a strong diurnal cycle of velocity differences of more than 10 cm s^{-1} is observed.
- Wind speed controls amplitude and timing of the diurnal cycles of shear and stratification in the upper 20 m of the equatorial Atlantic.
- Wind speed dependence of descent rates of diurnal shear and stratification can explain the varying onset of deep-cycle turbulence.

Abstract

The diurnal cycles of near-surface shear and stratification, also known as diurnal jet and diurnal warm layer (DWL), are ubiquitous in the tropical oceans, affecting the heat and momentum budget of the ocean surface layer, air-sea interactions, and vertical mixing. Here, we analyse the presence and descent of near-surface diurnal shear and stratification in the upper 20 m of the equatorial Atlantic as a function of wind speed using ocean current velocity and hydrographic data taken during two trans-Atlantic cruises along the equator in autumn 2019 and spring 2022, data from three types of surface drifters, and data from PIRATA moorings along the equator. The observations during two seasons with similar wind speeds but varying net surface heat fluxes reveal similar diurnal jets with an amplitude of about 0.11 m s^{-1} and similar DWLs when averaging along the equator. We find that higher wind speeds lead to earlier diurnal peaks, deeper penetration depths, and faster descent rates of DWL and diurnal jet. While the diurnal amplitude of shear is maximum for intermediate wind speeds, the diurnal amplitude of stratification is maximum for minimal wind speeds. The presented wind dependence of the descent rates of DWL and diurnal jet is consistent with the earlier onset of deep-cycle turbulence for higher wind speeds. The DWL and the diurnal jet not only trigger deep-cycle turbulence but are also observed to modify the wind power input and thus the amount of energy available for mixing.

Plain Language Summary

Variations in solar radiation over the course of the day cause a diurnal cycle of temperature, stratification, current velocity, and velocity shear in the near-surface ocean. These diurnal cycles are ubiquitous in the tropical oceans and are important for understanding the heat and momentum budget of the ocean surface layer and for understanding vertical mixing. Here, we analyse the diurnal cycles of stratification and velocity shear in the upper 20 m of the equatorial Atlantic, focussing on their presence, depth structure, and wind dependence. We use data taken during two trans-Atlantic cruises along the equator in autumn 2019 and spring 2022, data from surface drifters, and data from mooring sites along the equator. These observations indicate that the wind speed influences the amplitude, timing, and vertical structure of the diurnal cycles. The wind speed dependence of the depth propagation of the diurnal cycles of stratification and velocity shear is consistent with the wind speed dependence of mixing below the mixed layer. We further

show that the diurnal cycle of near-surface current velocities also leads to a diurnal cycle of the amount of wind energy released into the ocean.

1 Introduction

Oceanic parameters vary close to the surface with the diurnal cycle of solar radiation, including stratification, shear, and mixing. After sunrise, a diurnal (buoyantly isolated) warm layer (DWL) forms that traps heat and also wind-forced momentum close to the surface, creating a highly-sheared near-surface diurnal jet due to the 'slippery layer' effect. The stratified shear layer descends during late afternoon and evening, transmitting heat and momentum below the mixed layer into the deeper ocean. After sunset, cooling of the sea surface and convective overturning destroy the DWL (Kudryavtsev & Soloviev, 1990; Price et al., 1986; Smyth et al., 2013; Woods & Strass, 1986). This diurnal variability of shear and stratification is linked to diurnal variability of turbulent dissipation both within the DWL (St. Laurent & Merrifield, 2017; Sutherland et al., 2016) and below (Moum et al., 2022; Peters et al., 1988). Therefore, the near-surface diurnal cycle modifies near-surface heat and momentum budgets and plays a role in air-sea interactions and vertical mixing.

Understanding the diurnal cycle is of particular interest in equatorial regions for several reasons:

1. The equatorial Atlantic and Pacific are characterised by a zonal current system and a highly-sheared Equatorial Undercurrent (EUC), eventually leading to the presence of marginal instability. Marginal instability is defined as a state in which shear and stratification vary almost proportionally so that the Richardson number remains close to its critical value (Smyth & Moum, 2013; Smyth et al., 2019). It is observed in the equatorial Pacific that, when the descending diurnal shear layer merges with the marginally unstable shear above the EUC core, shear instabilities are induced that can trigger turbulence, the so-called deep-cycle turbulence (DCT) (Smyth & Moum, 2013; Smyth et al., 2013; Pham et al., 2013). DCT also occurs in the equatorial Atlantic, but it is still an open question whether there are fundamental differences in the nature of instabilities leading to DCT in the Atlantic and Pacific (Moum et al., 2023).

2. Diurnal jet and DWL are observed to reach and thus impact the ocean far deeper near the equator than away from it (Masich et al., 2021). This discrepancy arises due to a combination of Coriolis rotational effects that are vanishing towards the equator disabling the rotation of horizontal velocities with depth (Hughes et al., 2020a) and the presence of very high background shear near the equator supporting the descent of the shear layer (e.g., Lien et al., 1995). Note that longitudinal differences in background shear and the presence of marginal instability can also lead to longitudinal differences in the penetration depth of the diurnal jet (Masich et al., 2021).
3. Equatorial cold tongue regions are critical for the global heat balance and the near-surface diurnal cycle presents a key mechanism there for the heat uptake from the atmosphere to the stratified ocean below the surface mixed layer (Moum et al., 2013; Whitt et al., 2022). Upwelling and mixing in these regions define not only the downward heat flux but similarly the upward nitrate flux (Radenac et al., 2020; Brandt et al., 2023), stressing the importance of diurnal variability at the equator also for biological productivity.
4. It is expected that in the tropics and subtropics, which often present a larger partial pressure of CO_2 in the ocean than in the atmosphere, diurnal variability of turbulence within the DWL increases the flux of CO_2 from the ocean to the atmosphere (Sutherland et al., 2016).

Wind speed influences the formation and the pattern of the DWL and the diurnal jet as indicated by observational (Hughes et al., 2020b; Wenegrat & McPhaden, 2015; Masich et al., 2021) and modelling studies (Hughes et al., 2020a, 2021), where the diurnal cycle of the wind itself can be neglected as it is at least one order of magnitude smaller than the daily-mean wind signal magnitude (Masich et al., 2021; Smyth et al., 2013). It has been suggested that DWLs and diurnal jets do not exists for wind speeds exceeding a threshold ranging between 6 m s^{-1} and 8 m s^{-1} (Hughes et al., 2021; Kudryavtsev & Soloviev, 1990; Matthews et al., 2014; Thompson et al., 2019). Furthermore, Wenegrat & McPhaden (2015) observed a seasonal variability in the equatorial Atlantic with pronounced descending diurnal shear layers and limited diurnal sea surface temperature variability in steady trade wind conditions during boreal summer and autumn, and opposite patterns in weak wind conditions during boreal winter and spring. More

comprehensive analyses of the interaction between the wind and DWL and diurnal jet have been performed in the tropical Pacific. For higher wind speeds, the penetration depth of both DWL and diurnal jet becomes deeper (Hughes et al., 2020b; Masich et al., 2021; Price et al., 1986), and the descent rate of the DWL increases (Hughes et al., 2020b). However, little is known about the diurnal amplitudes as a function of wind speed. Masich et al. (2021) found a linear relationship between the wind speed and the strength of the diurnal cycle of current velocities at locations where marginal instability was present. Price et al. (1986) suggested that the diurnal jet amplitude is solely dependent on the net surface heat flux and followingly independent of the wind speed. Hence, there is a lack of a comprehensive analysis of the interplay between wind and diurnal jet regarding descent rates and diurnal amplitudes as well as a lack of a confirmation of the processes observed in the tropical Pacific for the tropical Atlantic.

Measurements of ocean currents in the upper 10 m are still rare because of measurement constraints and noise, e.g., shipboard measurements with acoustic Doppler current profilers (ADCP) typically cover a depth range below 15 m depth and moored measurements with upward looking ADCPs are contaminated by interference with surface reflections or aggregation of fish (Röhrs et al., 2021; Elipot & Wenegrat, 2021). However, near-surface estimates within the upper 10 m are necessary to properly capture the diurnal dynamics. Only few studies provide observational estimates within the upper 10 m at diurnal time scales. These studies are located in the tropics to subtropics and are based on different types of surface drifters (Kudryavtsev & Soloviev, 1990), on current meters and/or ADCPs attached to a mooring or surface buoy (Price et al., 1986; Cronin & Kessler, 2009; Wenegrat & McPhaden, 2015; Sutherland et al., 2016; Pham et al., 2017), or on a SurfOtter (Hughes et al., 2020a). The resulting diurnal jet amplitudes vary from 10 cm s^{-1} to 20 cm s^{-1} with different associated depth intervals, different locations as well as different seasons and prevailing background conditions. The vertical structure of near-surface shear and factors influencing the diurnal jet are still poorly understood.

This study combines observational data sets from the TRATLEQ expeditions, which are two trans-Atlantic equatorial cruises with dedicated en-route measurements and drifter deployments, and data sets from specially-instrumented PIRATA moorings to capture diurnal stratification and shear in the upper 15 m of the equatorial Atlantic Ocean. With these data sets, we aim to assess near-surface diurnal dynamics focussing on the influence of background conditions and, in particular, on the wind speed dependency. Followingly, the study addresses

the lack of near-surface measurements and the knowledge deficit about the wind dependency of diurnal jet and the DWL in the equatorial Atlantic. The paper is organised as follows. Data and methodology are described in sections 2 and 3, respectively. Results about the near-surface diurnal cycle in the equatorial Atlantic and impacts of different background conditions are presented in section 4. The impact of the wind speed on diurnal shear and stratification is examined in more detail in section 5. The results are then discussed in terms of descent rates of diurnal shear and stratification and are linked to the wind dependence of DCT found by Moum et al. (2023) in section 6.1. The impact of the described diurnal cycles on the wind power input (WPI) is discussed in section 6.2.

2 Observational data

This study focusses on different observational data sets from the TRATLEQ expeditions, consisting of two research cruises and associated surface drifter experiments, and data sets from PIRATA moorings (Figure 1).

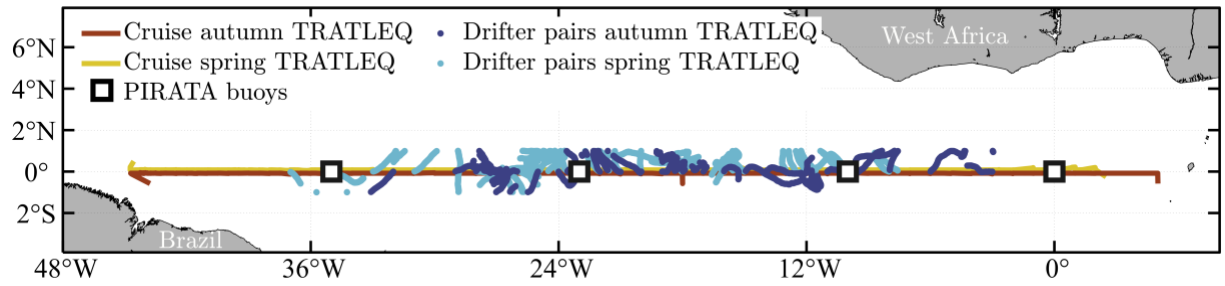

Figure 1. Geographical map of the observations used in the present study. Displayed are mean positions of drifter pairs within 1° north and south of the equator deployed during TRATLEQ I in autumn 2019 (dark blue dots) and TRATLEQ II in spring 2022 (light blue dots), the equatorial transects of the autumn (red line) and spring (yellow line) TRATLEQ cruises, and the locations of the PIRATA buoys (black-bordered squares).

2.1 TRATLEQ Cruises

Shipboard measurements were carried out during the cruises M158 and M181 with the research vessel Meteor, the so-called TRATLEQ (Trans-Atlantic Equatorial) cruises I & II. The cruises provide equatorial Atlantic transects from 5°E to 45°W between September 29 and October 22, 2019 and from 2°E to 45°W between April 30 and May 20, 2022. In the following, TRATLEQ I will be termed (boreal) autumn TRATLEQ and TRATLEQ II (boreal) spring TRATLEQ. During both cruises, near-surface stratification is estimated from 10 s sea surface

temperature and sea surface salinity measurements by the ship's dual thermosalinograph (TSG) as well as 10 s pitch and roll data from the ship (more details in section 3.2). The vessel measures the speed and direction of the wind at 30 m height as well as global short-wave radiation (SWR) with a temporal resolution of 1 min. Direct shipboard velocity measurements from a marine radar and a vessel-mounted ADCP (vmADCP) are only considered for autumn TRATLEQ. A coherent-on-receive marine X-band (9.4 GHz) radar developed at the Helmholtz-Zentrum Hereon (Horstmann et al., 2021) was installed during autumn TRATLEQ. The instrument was set to operate at a pulse length of 50 ns (i.e., short-pulse mode), providing a range resolution of 7.5 m. It is equipped with a vertical transmit and receive (VV) polarised antenna of 2.3 m (7.5 ft) with a beam width of 1.1°, a rotational period of 2 s and a pulse repetition frequency of 2 kHz. The obtained image sequences are analysed with respect to the surface wave properties such as wave directions, wave lengths, and phase velocities. The surface current vector is then resulting from the difference between the observed phase velocities and the phase velocities given by the linear dispersion relation of surface gravity waves (Horstmann et al., 2015; Lund et al., 2018). The retrieved surface current layer varies between 1 m and 5 m depth, depending on the surface wave length. Here, a mean depth of 3 m is assumed for the marine Radar measurements. A validation study in the Gulf of Mexico showed a root-mean-square error of 4 cm s^{-1} compared to velocities of surface drifters representing the upper 0.4 m depth (Lund et al., 2018). There are no data between 18°W and 25°W, that is, from October 09 to October 12, 2019 and only data between 0°0.6' S and 0°0.6' N are considered. In addition to the marine radar, a vmADCP, a 75 kHz RDI Ocean Surveyor, was installed during autumn TRATLEQ with the bin size set to 8 m (Brandt et al., 2022). Here, only data from the uppermost bin centred at 17 m depth are considered. Hourly velocity data from the vmADCP have an accuracy of 1 cm s^{-1} for on-station and 2-4 cm s^{-1} for underway measurements depending on wave and wind conditions (J. Fischer et al., 2003). For comparison of marine radar and vmADCP data, 10 min averages were calculated. Outliers of the velocity differences between the two data sets were determined using a criterion of three standard deviations off the median and were eliminated. Direct shipboard velocity measurements are not considered for spring TRATLEQ. Due to a malfunction of the OS75kHz system (vmADCP), a 75kHz LR was installed in the sea chest during that cruise, which had a reduced signal-to-noise ratio for the uppermost bin, leading to a distortion of the diurnal cycle.

196 ### 2.2 TRATLEQ drifter experiments

197 During both TRATLEQ cruises, drifter experiments were carried out that consisted of the
198 pairwise deployments of two types of surface drifters about every 1° longitude along the equator.
199 For autumn TRATLEQ, 31 SVP (Surface Velocity Program) drifters, drifting with velocities at
200 about 15 m depth, and 27 CARTHE (Consortium for Advanced Research on Transport of
201 Hydrocarbon in the Environment) drifters, providing velocities at about 0.5 m depth, were
202 deployed between September 29 and October 18, 2019. For spring TRATLEQ, 18 SVP drifters
203 and 44 Hereon drifters, which are similar to CARTHE drifters and provide velocities at about 0.5
204 m depth, were deployed between May 04 and May 17, 2022. Both trajectory data sets were
205 quality-controlled and interpolated to hourly values. Estimates of the velocity difference between
206 0.5 m and 15 m were then based on drifter pairs that are separated in time by less than 1 hour and
207 in distance by less than 100 km (details in Text S1 and Figure S1). This study considers 7633
208 drifter pairs between October 02 and October 29, 2019 in the area from 33°W to 3°W and 1°S to
209 1°N as well as 9602 drifter pairs between May 04 and June 02, 2022 in the area from 37°W to
210 8°W and 1°S to 1°N. The mean distance of the paired drifters is 46 km for autumn TRATLEQ
211 and 54 km for spring TRATLEQ.

212 ### 2.3 PIRATA moorings

213 Near-surface temperature and salinity data from the PIRATA (Prediction and Research
214 Moored Array in the Tropical Atlantic) buoys at 0°N, 23°W and 0°N, 10°W are used. Moorings
215 were progressively equipped with temperature and conductivity sensors at 1 m, 5 m, 10 m, 20 m,
216 and 40 m depth from 1999 to 2022. Wind data at 4 m height are taken from the PIRATA sites
217 0°N, 0°W (1999 - 2022), 0°N, 10°W (1999 - 2022), 0°N, 23°W (1999 - 2022), and 0°N, 35°W
218 (1998 - 2022) (Bourlès et al., 2019). The net surface heat flux at 0°N, 10°W and 0°N, 23°W is
219 estimated as the sum of SWR, long-wave radiation, latent, and sensible heat flux provided by
220 ePIRATA (Foltz et al., 2018) for the two TRATLEQ periods. Additionally, a Teledyne-RDI
221 Sentinel Workhorse 600 kHz ADCP was deployed at 0°N, 23°W from October 13, 2008 until
222 June 18, 2009, providing hourly velocity averages from a depth of 4.3 m to 38.8 m (see
223 Wenegrat et al., 2014). The data set is masked according to
224 (https://www.pmel.noaa.gov/tao/drupal/disdel/adcp_0n23w/index.html). This period of near-

surface high vertical resolution moored velocity measurements will be referred to as enhanced monitoring period (EMP).

2.4 Satellite wind data

Winds at 10 m height are taken from the gridded 6-hourly Cross-calibrated Multi-Platform (CCMP) near-real time wind satellite product provided by Remote Sensing Systems for the period January 2000 to November 2022. The product is also used to estimate the wind at the drifter locations. The CCMP V2.0 product is processed to L3 standard, has a horizontal resolution of 0.25° x 0.25° and a temporal resolution of 6 h. It is averaged daily for the following analysis.

3 Methods

3.1 Stratification from the PIRATA moorings

For the PIRATA moorings, temperature and salinity data are given on regular pressure and time grids. The stratification, N^2, is given as squared Brunt-Väisälä frequency and can be calculated according to IOC et al. (2010) as

$$N^2 = g^2 * \rho * \frac{\beta * \Delta S_A - \alpha * \Delta \theta}{\Delta P} \quad (1)$$

where θ is the conservative temperature, S_A the absolute salinity, ρ the in-situ density, g the gravitational acceleration, α and β the coefficients of thermal expansion and saline contraction, respectively, and P the pressure in Pa. The respective parameters are computed using the Gibbs SeaWater Oceanographic Toolbox of TEOS-10.

3.2 Stratification from the vessel-mounted thermosalinograph

The stratification, N^2, at the depth of the TSG inlet can be estimated using data taken at a high sampling rate (here 0.1 s^{-1}) for temperature, salinity, and the vertical movement of the inlet position relative to the water column. This method was first described in T. Fischer et al. (2019). The vertical distance of the inlet relative to the mean sea level is evaluated as

$$d_{inlet,sealevel} \approx \left(y_{inlet,com} * \sin(\psi) - z_{inlet,com} * \cos(\psi)\right) * \cos(\gamma) - x_{inlet,com} * \sin(\gamma) + d_{com,sealevel} \quad (2)$$

where $(x, y, z)_{inlet,com}$ is the inlet position relative to the center of mass in ship's coordinates, positive for (bow, starboard, up), and $d_{com,sealevel}$ is the distance of the center of mass to sea level. For the RV Meteor III, $(x, y, z)_{inlet,com}$ = (40 m, -3 m, -2 m) and $d_{com,sealevel}$ = 1 m. Moreover, ψ is the roll angle positive for starboard down, and γ is the pitch angle positive for bow up. This calculation is only an estimate, being accurate to at least the order. Not considered are surface waves and the actual flow along the ship's hull which causes uncertainties in the actual depth of the sampled water and in the measured properties. The mean $d_{inlet/sealevel}$ is 4.1 m ± 0.4 m during the equatorial section of autumn TRATLEQ and 4.0 m ± 0.4 m during the equatorial section of spring TRATLEQ. Neglecting ΔS_A in Equation (1), N^2 at the inlet can be approximated to

$$N^2 \approx g^2 * \rho * \alpha * \frac{T_z}{10^4} \; with \; T_z = \frac{\sqrt{var(T)}}{\sqrt{var(d_{inlet,sealevel})}} \quad (3)$$

where T_z is the vertical temperature gradient and T is the temperature measured at the TSG inlet.

3.3 Vertical shear of horizontal velocities

In this study four different velocity data sets are considered: 1. Marine radar and vmADCP data during autumn TRATLEQ, 2. CARTHE and SVP drifter experiment during autumn TRATLEQ, 3. Hereon and SVP drifter experiment during spring TRATLEQ, and 4. the EMP at the PIRATA site 0°N, 23°W. For all four data sets, the zonal and meridional ocean velocities are transformed into an along- and across-wind coordinate system. This transformation allows an easier identification of the diurnal jet as, according to its definition, the jet is created by wind that is trapped in the DWL. A positive across-wind component corresponds to velocities to the left of the wind direction. The chosen wind value (satellite winds for 1-3, PIRATA winds for 4) is the daily-mean value that is closest in time and space to the velocity measurements. The vertical shear of horizontal velocities in along-wind direction, Sh_{Al}, is defined as the vertical derivative of the along-wind velocities. In the following, vertical differences of horizontal velocities and Sh_{Al} are considered as defined above.

3.4 Diurnal cycle diagnostics

Mean diurnal cycles are created by taking the mean of hourly bins. The time is considered in Solar Apparent Time (SAT) so that solar noon is centred at 12:00, using a conversion from Universal Time Coordinated to SAT (Koblick, 2021). The standard error is

computed as $\frac{std}{\sqrt{f}}$ where *std* is the standard deviation and for the degrees of freedom, f, one independent value per day is assumed. Diurnal patterns are compared in terms of the diurnal timing and the diurnal amplitude. The peak (timing and value) is determined by a sinusoidal fit $f(t) = \alpha * \sin(\omega * t + \varphi)$ as a function of time t [days] considering ± 3.5 h around the maxima of the hourly means (i.e., 7 values of the hourly time series are used). Only periods ($\frac{2*\pi}{\omega}$) between 0.5 and 2 days and phases (φ) smaller than 1 day are considered. A symmetric fit is assumed to be a good enough approximation, though there might be a tendency for a slower increase and a faster decrease. The amplitude is calculated as the difference of the peak value determined by the fit and the minimum of the hourly means between 6:00 SAT (sun rise) and the peak time. These two characteristics are calculated for all robust diurnal cycles where the robustness is determined using a signal-to-noise ratio. The signal is defined as the amplitude, and the noise is defined as the arithmetic mean of the hourly computed standard errors. If the signal-to-noise ratio exceeds 2.5 for Sh_{Al} and 10 for N^2, we assume the presence of a robust diurnal cycle for Sh_{Al} and N^2 as well as the presence of a DWL and a diurnal jet, respectively. In order to determine the accuracy of the sinusoidal fits, the bootstrapping method is utilised. This allows to establish confidence intervals (CI) for the estimated parameters without prior knowledge of the shape of the underlying distribution (Efron, 1979). For each diurnal fit, 10,000 resamples are taken from the original data set with replacement and the same probability for each datapoint to be selected. Each set of resamples has the sample size of the original data set. From the resulting distribution of parameters for the diurnal fit, a 95% CI is given by taking the 2.5% and 97.5% quantiles.

3.5 Wind speed, wind stress, and wind power input

For comparability, the shipboard wind measurements from the TRATLEQ cruises in 30 m height and the PIRATA buoy wind measurements in 4 m height are scaled to 10 m wind velocities using a logarithmic wind profile for neutral conditions. For a given height, z, the 10 m winds can be calculated as

$$W(10\ m) = W(z) * \frac{\ln(10\ m) - \ln(z_0)}{\ln(z) - ln(z_0)} \quad (4)$$

where *W* is the wind velocity and z_0 the surface roughness length (Fleagle & Businger, 1980) with offshore assuming $z_0 = 0.0002$ (Dutton, 1995). In the following, the horizontal wind vector

307 at 10 m height is denoted as $\boldsymbol{u_{10}}$. The wind stress vector, $\boldsymbol{\tau}$, is then defined as (Pacanowski,
308 1987)

309 $$\boldsymbol{\tau} = \rho_a * c_D * (\boldsymbol{u_{10}} - \boldsymbol{u}) * |\boldsymbol{u_{10}} - \boldsymbol{u}| \qquad (5)$$

310 where $\rho_a = 1.223\ kg\ m^{-3}$ is the density of air, $c_D = 0.0013$ the drag coefficient, and $\boldsymbol{u}$ the
311 observed ocean surface velocity vector.

312 The WPI is the mechanical energy transferred by winds into the ocean. Part of this energy
313 drives upper-ocean turbulence and is locally dissipated (Moum & Caldwell, 1985). The wind
314 stress works on the ocean flow, so that the WPI is defined as

315 $$WPI = \boldsymbol{\tau} * \boldsymbol{u} * \rho_w^{-1} \quad (6)$$

316 where $\rho_w = 1025\ kg\ m^{-3}$ is the density of sea water. Note that ignoring the effect of the ocean
317 surface velocity on $\boldsymbol{\tau}$, i.e. using $\boldsymbol{u_{10}}$ instead of the velocity difference ($\boldsymbol{u_{10}}$ - $\boldsymbol{u}$) in Equation (5),
318 leads to a 3% / 5% / 6% increase in the mean $\boldsymbol{\tau}$ if $\boldsymbol{u}$ were velocities at 0.5 m depth from the
319 CARTHE drifters / velocities at 0.5 m depth from the Hereon drifters / velocities at 4.3 m depth
320 of the EMP at 0°N, 23°W. This increase is derived using daily-mean wind speeds and hourly
321 ocean velocities.

4 Diurnal cycle in the equatorial Atlantic during two contrasting seasons

4.1 Background conditions

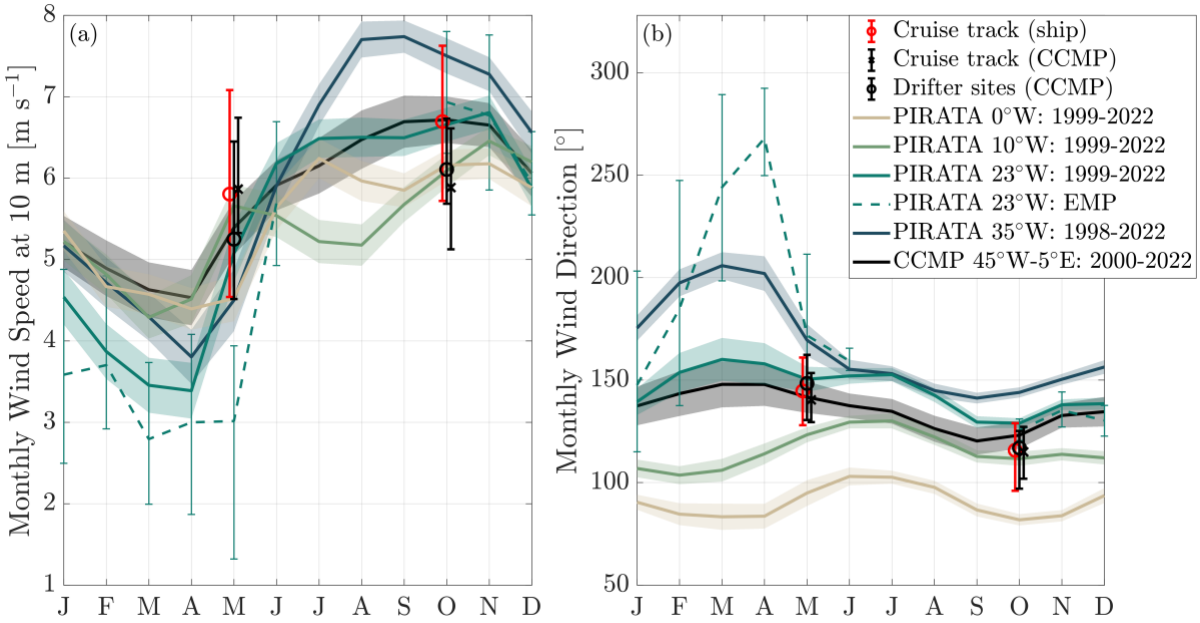

Figure 2. Seasonal wind climatologies for the equatorial Atlantic and wind conditions during measurement campaigns. Mean seasonal (a) wind speed at 10 m height and (b) wind direction in polar coordinates (0° corresponds to westerlies, 90° to northerlies) derived from wind measurements at four different PIRATA sites (coloured lines) and from CCMP winds (black lines) at the equator. The dashed line corresponds to PIRATA winds measured at 0°N, 23°W during the EMP (from October 2008 until June 2009). Values for the TRATLEQ expeditions are derived from the ship's sensors along the cruise tracks (red circle) and by interpolating CCMP winds on the drifter (black cross) and ship positions (black circle). Shading denotes ± one standard error of the monthly mean assuming one independent value per month, and error bars denote the interquartile range.

Wind and net surface heat flux are assumed to potentially govern the pattern of the diurnal cycles of near-surface shear and stratification. We start by investigating these two atmospheric fields as background conditions to classify diurnal shear and stratification obtained during the two TRATLEQ expeditions.

Monthly climatologies of wind speed and direction in the equatorial Atlantic are derived from PIRATA buoys at four different longitudes and from the CCMP product zonally averaged between 45°W and 5°E, using the complete available time series (Figure 2). The CCMP winds

have a clear seasonal cycle with a minimum speed of 4.5 m s^{-1} in April and a maximum speed of 6.7 m s^{-1} in October associated with the meridional migration of the Intertropical Convergence Zone (Waliser & Gautier, 1993). The wind is directed towards the northwest, ranging from 120° (SSE) in September to 148° (SE) in March. CCMP winds along the equator are mostly consistent with PIRATA measurements at 23°W and 10°W. The PIRATA measurements further indicate that whilst the amplitude of seasonal variations in wind speed and direction is decreasing from the western to the eastern basin, the wind direction is changing from dominantly easterlies to dominantly southerlies across the basin.

This seasonal wind variability is the main reason for the different wind conditions that prevail during the two TRATLEQ expeditions in boreal autumn 2019 and boreal spring 2022, shown as zonal means in Figure 2. Three wind estimates are provided to determine wind conditions during the TRATLEQ expeditions: an average of the wind from the ship's sensors during the TRATLEQ cruises and averages of the CCMP product interpolated on the ship as well as drifter positions. The mean wind speed differed by 0.9 m s^{-1} between the two cruises considering both CCMP and ship's sensor winds. The mean wind speed at the location of the drifter pairs is the same for the two experiments with similar wind conditions for the cruise and associated drifter experiment during autumn TRATLEQ and an offset of 0.6 m s^{-1} during spring TRATLEQ. The mean wind direction changed about 30° between the two cruises and between the two drifter experiments, yielding more northward (meridional) winds for spring TRATLEQ and more westward (zonal) winds for autumn TRATLEQ. A comparison of the conditions during the TRATLEQ expeditions with the zonal mean CCMP climatology suggests that the observed wind direction was typical and the wind speed atypical with respect to the climatological seasonal cycle. Note further that the mean CCMP wind speed is 0.6 m s^{-1} lower than the mean ship's sensor wind speed for both cruises, possibly pointing to a general offset between the directly measured wind speed and the CCMP product.

The net surface heat flux is computed as the sum of SWR, long-wave radiation, latent, and sensible heat flux. While the mean SWR differs only by 14 W m^{-2} between the two cruises, there is a higher difference between the drifter experiments. Averaging the SWR measured at the PIRATA buoys at 0°N, 10°W and 0°N, 23°W for the periods of the two drifter experiments

yields 31 W m^{-2} (14 %) higher SWR during autumn compared to spring TRATLEQ. The net surface heat flux is higher by 39 W m^{-2} (45 %) respectively.

Hence, the two TRATLEQ periods are characterised by comparable mean wind speeds for the two drifter experiments and a difference in mean wind speeds of 0.9 m s^{-1} between the two cruises. The mean wind direction is shifted by about 30° comparing both the drifter experiments and cruises. Furthermore, the net surface heat flux is noticeably weaker and the SWR slightly weaker during spring TRATLEQ compared to autumn TRATLEQ.

4.2 Observed near-surface diurnal shear

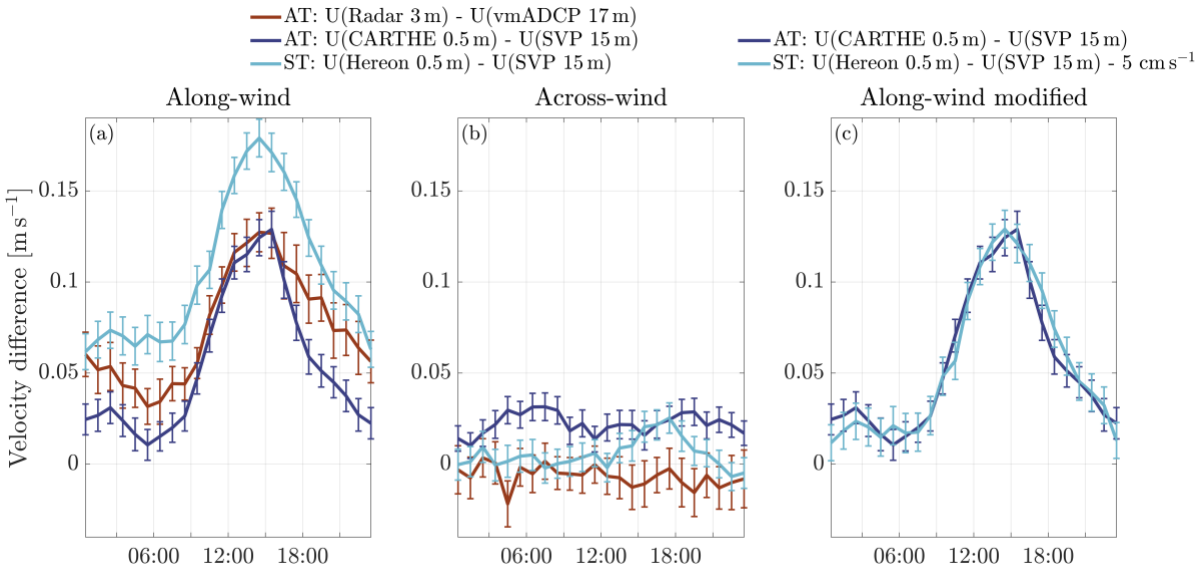

Figure 3. Mean diurnal cycles of vertical differences of horizontal velocities in (a) along- and (b) across-wind direction as a function of SAT. The velocity differences are obtained from the marine radar and the uppermost bin of the vmADCP during autumn TRATLEQ (AT, dark red) and from the drifter experiments during autumn TRATLEQ (AT, dark blue) and spring TRATLEQ (ST, light blue). Further, (c) compares the drifter experiments in (a) with a background velocity difference of 0.05 m s^{-1} removed for spring TRATLEQ. The error bars represent the standard error.

The mean diurnal cycles of vertical differences of horizontal velocities are investigated close to the surface, measured between 0.5 m and 15 m depth by CARTHE/Hereon and SVP drifters and between 3 m and 17 m depth by the marine radar and the vmADCP (Figure 3). For all data sets, there are stronger diurnal and background signals in the along-wind component than

388 in the across-wind component (Figure 3a,b), implying that the vertical differences of near-
389 surface velocities are mainly wind driven. Therefore, only the along-wind component is
390 considered in the following. A clear diurnal cycle is seen in the along-wind velocity differences
391 (Figure 3a). Velocity differences are at their minimum in the morning hours (from 0:00 to 6:00
392 SAT), increase after sunrise (6:00 SAT) until they reach their maximum between 14:00 and
393 16:00 SAT (2 – 4 h after solar noon) and decrease in the evening - corresponding to the features
394 of a diurnal jet. This results in diurnal amplitudes of 11.8 cm s^{-1} (autumn TRATLEQ drifter), 9.6
395 cm s^{-1} (autumn TRATLEQ shipboard), and 11.7 cm s^{-1} (spring TRATLEQ drifter). For the
396 autumn TRATLEQ expedition, the diurnal amplitude obtained from the drifter experiment
397 exceeds the one from shipboard measurements by 22%. While the magnitude of velocity
398 differences is the same in the afternoon, there is a 2.0 cm s^{-1} weaker night-time velocity
399 difference for the drifter measurements compared to the shipboard measurements. Overall, the
400 two measurement techniques are in good agreement, showing the robustness of the diurnal cycle
401 and giving confidence in the usage of both techniques. The distance criterion of 100 km used for
402 the collocation of pairs of the two drifter types reveals that the diurnal cycle is also a horizontally
403 large-scale feature, matching previous findings (Bellenger & Duvel, 2009).

404 The drifter experiments during the autumn and spring TRATLEQ expeditions yield
405 closely resembling diurnal cycles for the vertical differences of horizontal velocities between 0.5
406 m and 15 m depth (Figure 3c). While the pattern of the diurnal cycles agrees well, there is an
407 offset of 5 cm s^{-1}. This offset can be better interpreted in terms of background shear when
408 looking at the western, central, and eastern basin separately (Table 1). Background shear is
409 analysed as the velocity difference between 0.5 m and 15 m depth averaged between midnight
410 and sunrise, that is, 0:00 to 6:00 SAT. During this period, the DWL and hence the diurnal jet are
411 removed by nocturnal mixing, and only the background shear remains. The seasonal and
412 longitudinal variations of this background shear yield a range from -0.4 cm s^{-1} to 11.8 cm s^{-1} in
413 the along-wind component with more zonal background shear during spring TRATLEQ and
414 more meridional background shear during autumn TRATLEQ. A comparison with the depth and
415 strength of the EUC, which was generally shallower and stronger during spring compared to

autumn TRATLEQ (Brandt et al., 2023), indicates that the presence of a higher zonal background shear goes along with a shallower and stronger EUC.

	Western: 37°W to 25°W	Central: 25°W to 17°W	Eastern: 17°W to 2°W
AT: wind speed [m s^{-1}], wind direction [°]	6.0 ± 0.7, 128 ± 15	6.0 ± 0.7, 116 ± 13	5.7 ± 1.1, 100 ± 18
AT: diurnal amplitude of along-wind velocity differences [cm s^{-1}]	13	13	12
AT: 0 – 6 SAT mean velocity difference along-wind (zonal, meridional) [cm s^{-1}]	-0.4 ± 1.6 (-3.2 ± 1.5, -3.1 ± 1.4)	3.5 ± 1.5 (-0.4 ± 1.3, 4.2 ± 1.5)	3.4 ± 1.2 (-3.7 ± 1.2, 1.3 ± 1.1)
ST: wind speed [m s^{-1}], wind direction [°]	6.1 ± 0.8, 158 ± 14	5.5 ± 1.2, 135 ± 32	6.0 ± 1.0, 127 ± 16
ST: diurnal amplitude of along-wind velocity differences [cm s^{-1}]	12	13	14
ST: 0 – 6 SAT mean velocity difference along-wind (zonal, meridional) [cm s^{-1}]	8.4 ± 2.2 (-9.2 ± 2.1, -0.1 ± 1.2)	1.2 ± 1.5 (-2.2 ± 1.7, 0.4 ± 1.7)	11.8 ± 1.4 (-9.2 ± 1.6, 7.3 ± 1.0)

Table 1: Background conditions in the western, central, and eastern equatorial Atlantic basin during the TRATLEQ drifter experiments. The mean CCMP wind speed and direction as well as the diurnal amplitude and the mean for the period 0:00 to 6:00 SAT of the velocity differences between 0.5 and 15 m depth are calculated for three

longitudinal groups during the autumn TRATLEQ (AT) and spring TRATLEQ (ST) drifter experiments. For the 0 – 6 SAT mean velocity difference, the zonal and meridional components are additionally given in brackets.

The meridional background velocity difference is strongest during phases of enhanced meridional winds, i.e., during autumn TRATLEQ and generally in the eastern basin. Marine radar and vmADCP measurements during the autumn TRATLEQ cruise reveal a strong positive correlation between the daily-mean meridional wind stress (ignoring the effect of the ocean surface velocity on τ) and the daily-mean vertical differences of meridional velocities, yielding a Pearson correlation coefficient of 0.81 using CCMP winds and 0.79 using ship's sensor winds. These correlations are significant at the 99%-level according to a Student's t-test. The correlations imply that, directly at the equator, a higher meridional wind stress results in higher meridional background shear. This is in line with the presence of the equatorial roll which is a shallow cross-equatorial overturning cell in the upper 80 m of the ocean with northward surface flow and a velocity reversal at about 25 m depth (Heukamp et al., 2022).

The wind speed during both drifter experiments is comparable in the three basins, while the wind direction is turning 30° westward from the eastern to the western basin. Like the wind speed, the diurnal amplitudes are comparable across the basin (Table 1).

These results suggest that the seasonal and longitudinal differences in background conditions mainly impact the background shear. With the wind speed being the only considered background condition that was similar for both TRATLEQ drifter experiments, the wind speed

might control the strength of the diurnal amplitude, i.e. the diurnal jet. This hypothesis about the wind speed influence will be tested in section 5.

4.3 Observed near-surface diurnal stratification

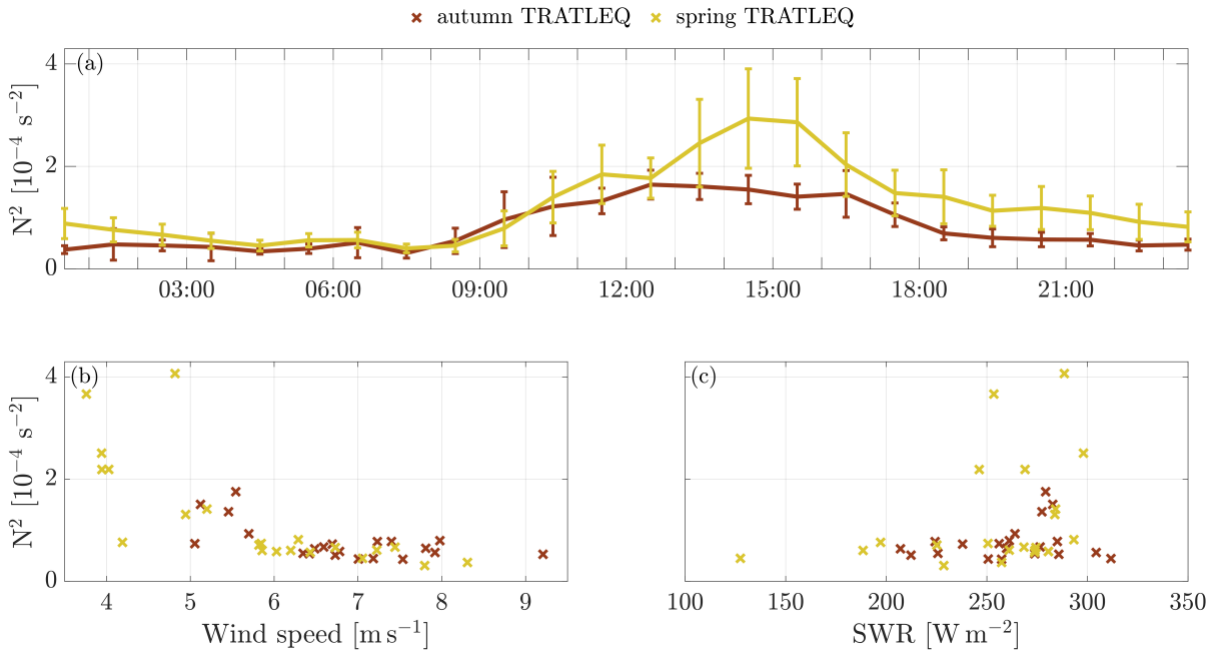

Figure 4. Stratification (N^2) at 4 m depth as a function of SAT, wind speed, and SWR. Mean diurnal cycles of N^2 are shown (a) as a function of SAT. The daily-mean N^2 is shown as a function of (b) wind speed at 10 m height and (c) SWR. All parameters are derived from shipboard measurements during the spring (yellow) and autumn (red) TRATLEQ cruises. The error bars in (a) represent the standard error.

Both cruises are also characterised by a diurnal cycle of near-surface stratification (N^2) estimated at a depth of about 4 m which shows weak stratification at night and maximum stratification in the afternoon (Figure 4a), indicating the presence of a DWL for both cruises. More precisely, the stratification is weakest about 1.5 h after sunrise and reaches its maximum 0.5 h (autumn TRATLEQ) to 2.5 h (spring TRATLEQ) after solar noon. While the diurnal cycles calculated for the two cruises are aligned during the morning hours, there is higher near-surface stratification in the afternoon and at night for spring TRATLEQ compared to autumn

TRATLEQ. Maximum and minimum N^2 are 1.6 * 10^{-4} s^{-2} and 0.3 * 10^{-4} s^{-2} for autumn TRATLEQ and 2.9 * 10^{-4} s^{-2} and 0.4 * 10^{-4} s^{-2} for spring TRATLEQ.

The effect of wind speed and SWR on daily-mean N^2 is shown in Figure 4b,c including the contribution of both the diurnal amplitude and night-time values. There are strong negative Pearson correlation coefficients between daily-mean wind speed and daily-mean stratification of -0.60 for autumn TRATLEQ and -0.73 for spring TRATLEQ, which are significant at the 99%-level according to a Student's t-test, suggesting higher stratification for lower wind speeds and vice versa. Although the mean wind speed only differed by 0.9 m s^{-1} between the two cruises, days with low wind speeds (< 5 m s^{-1}) occurred only during spring TRATLEQ, resulting in a higher spread of daily-mean stratification values compared to autumn TRATLEQ (Figure 4b). This might also explain the higher N^2 maximum for spring compared to autumn TRATLEQ. Furthermore, there appears to be a wind speed threshold of about 6 m s^{-1} that separates the higher and lower spread of daily-mean stratification values. A higher spread of stratification values can also be found for higher SWR (Figure 4c). As the occurrence of high daily-mean stratification coincides with both the presence of low wind speeds and high SWR, the wind speed threshold can be interpreted as a threshold below which SWR becomes important. A similar wind speed threshold of 6 m s^{-1} was found off Peru for near-surface stratification to persist overnight, possibly creating multi-day near-surface stratification (T. Fischer et al., 2019). The effect of the wind speed on the diurnal stratification will be further analysed in section 5.

The observations indicate that a DWL and a diurnal jet were present during both TRATLEQ expeditions. While the diurnal cycles (amplitude and phase) of near-surface velocity differences were identical, the amplitude of diurnal near-surface stratification was larger for spring TRATLEQ compared to autumn TRATLEQ. In this comparison it should be noted that the mean wind speed of the two TRATLEQ drifter experiments, from which diurnal velocity cycles were derived, differed by only 0.2 m s^{-1} while the mean wind speed of the two TRATLEQ cruises, from which the diurnal stratification cycles were derived, differed by 0.9 m s^{-1}. Hence, the wind speed might determine the amplitudes of not only the diurnal jet, as hypothesised earlier, but also of the DWL. In the following, the influence of the wind speed on the diurnal

cycles of shear and stratification will be examined focussing mainly on longer-term observations from the PIRATA buoy at 0°N, 23°W.

5 Wind speed dependence of the diurnal cycles

In this section, we explore the dependence of the near-surface shear and stratification on wind speed. During the TRATLEQ drifter experiments, 98% of the observed daily-mean wind speeds ranged from 3.4 m s^{-1} to 7.7 m s^{-1} and during the EMP at the PIRATA buoy at 0°N, 23°W from 0.4 m s^{-1} to 9.3 m s^{-1}. The effect of the wind speed on mean diurnal cycles of Sh_{Al} is analysed by subsampling Sh_{Al} for each hour of the day into 1.5 m s^{-1} wind speed intervals for drifters and mooring data (Figure 5).

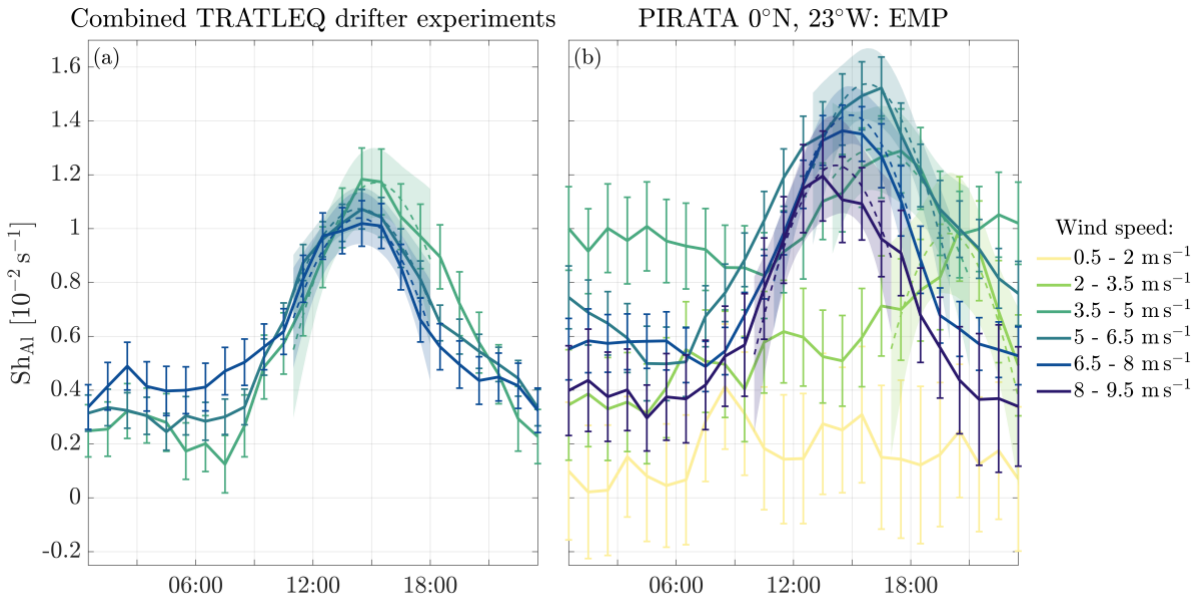

Figure 5. Mean diurnal cycles of along-wind shear (Sh_{Al}) as a function of SAT and wind speed. Sh_{Al} is derived (a) between 0.5 m and 15 m depth for both drifter experiments and (b) between 4.3 m and 14.8 m depth for the EMP at the PIRATA site at 0°N, 23°W. The colours correspond to different wind speed ranges. Wind speeds at 10 m height are taken from (a) CCMP and (b) PIRATA. For robust diurnal patterns, the peak is fitted to a sinusoidal function which is displayed by the dashed line. The error bars represent the standard error, and the shading marks the 95% CIs to estimate the fitted peak.

Diurnal cycles of Sh_{Al} averaged between 0.5 m and 15 m depth (4.3 m and 14.8 m depth) can be observed for winds stronger than 2 m s^{-1} as derived from the combined drifter experiments (the PIRATA EMP at 0°N, 23°W). With increasing wind speed, the diurnal peak occurs earlier and

tends to last for a shorter time. The latter relation indicates the tendency of a shorter persistence of the diurnal jet with higher wind speeds. The amplitude of the diurnal cycle of Sh_{Al} (Figure 5) varies between 4.7 (6.3) s^{-1} and 10.3 (10.5) $*10^{-3}$ s^{-1} with the maximum being reached at moderate winds of 5 m s^{-1} to 6.5 m s^{-1} (3.5 m s^{-1} to 5 m s^{-1}) considering the PIRATA EMP (combined TRATLEQ drifter experiments). Note that the difference of about 1.5 m s^{-1} in the wind speed at which maximum Sh_{Al} occurs in the two data sets might reduce considering the wind speed offset between the shipboard measurements and the CCMP winds of 0.6 m s^{-1}. The wind speed dependence of the diurnal pattern of Sh_{Al} is consistent in both data sets, though the associated differences in amplitude and timing are more distinct in the mooring data set. This might be a consequence of the larger range of seasons in the mooring data defining the distribution of not only wind speed but also other possible influencing parameters such as heat fluxes or near-surface Richardson number.

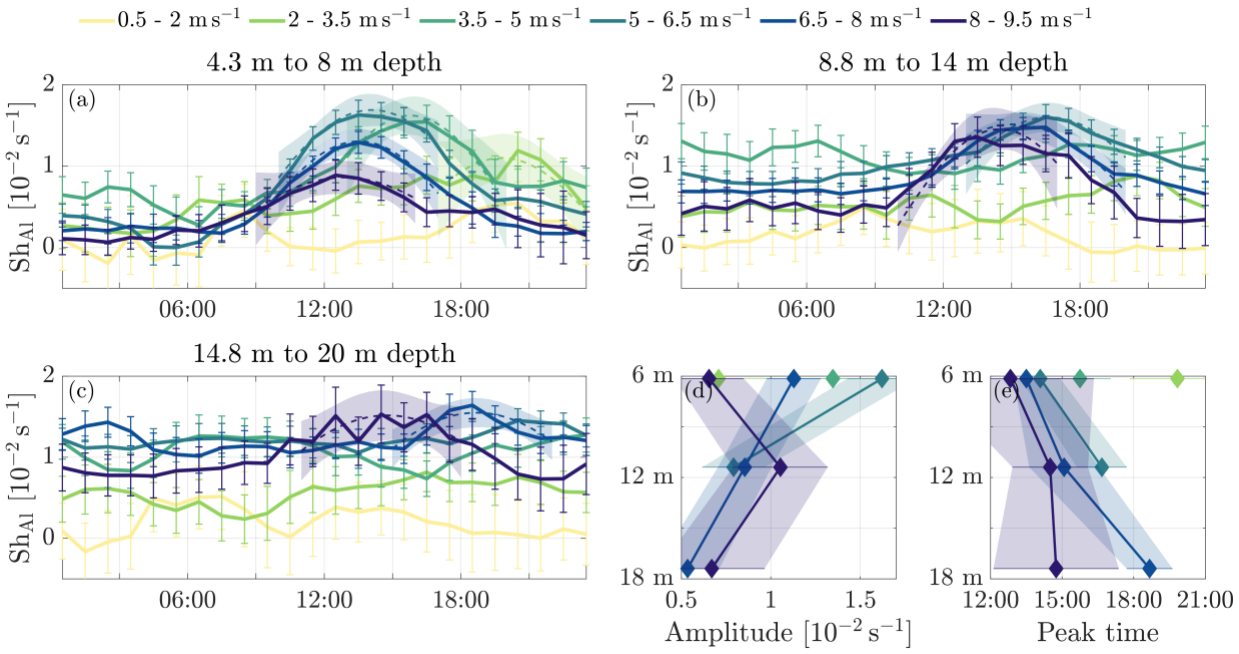

Figure 6. Mean diurnal cycles of along-wind shear (Sh_{Al}) as a function of SAT and wind speed. Sh_{Al} is derived between (a) 4.3 m and 8.0 m, (b) 8.8 m and 14.0 m and (c) 14.8 m and 20.0 m depth for the EMP at the PIRATA site at 0°N, 23°W. For robust diurnal pattern, the peak is fitted to a sinusoidal function which is displayed by the dashed line. For these cases, (d) the diurnal amplitude of Sh_{Al} and (e) the timing of the diurnal peak are displayed for the three different depth ranges. The colours correspond to different wind speed ranges. The vertical error bars represent the standard error, and the shading marks the 95% CIs to estimate the fitted peak.

To address the vertical structure and descent of the diurnal shear signal, Sh_{AI} is evaluated at 6.1 m depth (averaged between 4.3 m and 8.0 m, Figure 6a), 11.4 m depth (8.8 m and 14.0 m, Figure 6b), 17.4 m depth (14.8 m and 20.0 m, Figure 6c) as well as at 22.6 m depth (20.0 m and 25.3 m, not shown) derived from the PIRATA EMP at 0°N, 23°W. For the latter depth interval no wind group shows robust diurnal characteristics as defined in section 3.5. Wind speeds need to exceed 2 m s^{-1} for the diurnal jet to reach about 6 m depth, exceed 5 m s^{-1} to reach about 11 m depth, and exceed 6.5 m s^{-1} to reach about 17 m depth. While at 6 m depth the diurnal amplitude of Sh_{AI} (Figure 6d) is largest for moderate winds (as seen in Figure 6 for Sh_{AI} averaged for the upper 15 m depth), from 11 m depth downward, the diurnal amplitude increases with increasing wind speed. In general, the amplitude of Sh_{AI} decreases with depth for every wind group, except for 8 m s^{-1} to 9.5 m s^{-1} winds where the amplitude just reaches its maximum at 11 m depth. The diurnal peak of Sh_{AI} occurs later in the day with depth for all wind groups (Figure 6e), resulting in mean descent rates of 2.0 m h^{-1}, 2.2 m h^{-1}, and 5.9 m h^{-1} for wind speeds of 5 m s^{-1} to 6.5 m s^{-1}, 6.5 m s^{-1} to 8 m s^{-1}, and 8 m s^{-1} to 9.5 m s^{-1}, respectively.

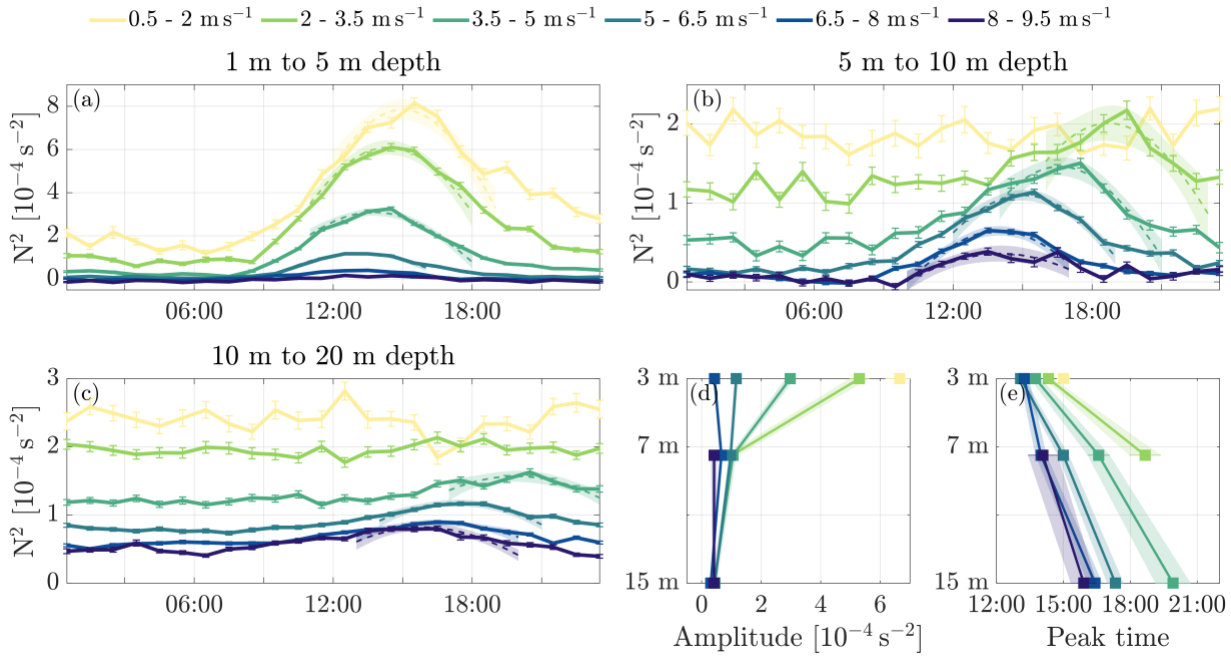

Figure 7. Mean diurnal cycles of stratification (N^2) as a function of SAT and wind speed. N^2 is derived between (a) 1 m and 5 m, (b) 5 m and 10 m, and (c) 10 m and 20 m depth for the PIRATA site at 0°N, 23°W. For robust diurnal patterns, the peak is fitted to a sinusoidal function which is displayed by the dashed line. For these cases, (d) the diurnal amplitude of Sh_{AI} and (e) the timing of the diurnal peak are displayed for the three different depth ranges.

The colours correspond to different wind speed ranges. The vertical error bars represent the standard error, and the shading marks the 95% CIs to estimate the fitted peak.

To address the vertical structure and descent of the diurnal stratification signal, N^2 is analysed at 3 m depth (averaged between 1 m and 5 m, Figure 7a), 7.5 m depth (10 m and 15 m, Figure 7b), 15 m depth (10 m and 20 m, Figure 7c), and 30 m depth (20 m and 40 m, not shown) derived from the PIRATA buoy at 0°N, 23°W. At all these depths N^2 increases with decreasing wind speed, valid all day through. The standard error also increases with decreasing wind speed, indicating a higher spread in N^2 values for weaker winds. This can be explained by the surface layer being more responsive to the heat flux at low wind speeds (Matthews et al., 2014). At 3 m depth, the diurnal cycle of N^2 (as described in section 4.3) is more pronounced with weaker wind speeds, reaching amplitudes of $6.7*10^{-4}$ s^{-2} for the weakest and $0.4*10^{-4}$ s^{-2} for the strongest wind group (Figure 7d). This relation between the diurnal amplitude of N^2 and the wind speed also applies to the other depths. However, the spread of the amplitudes reduces with depth. Wind speeds need to exceed 2 m s^{-1} for the DWL to reach about 7.5 m depth and exceed 3.5 m s^{-1} to reach about 15 m depth. There is no robust diurnal signal visible anymore at 30 m depth. Hence, the DWL reaches deeper for stronger winds but also becomes weaker. Besides, the wind affects the timing of the diurnal cycle with an earlier peak occurring for stronger winds (Figure 7e). The resulting spread of the peak times increases with depth. The descent of the maximum of N^2 becomes faster with increasing wind speeds with descent rates of 1.0 m h^{-1}, 1.9 m h^{-1}, 2.8 m h^{-1},

559 3.8 m h^{-1}, and 4.1 m h^{-1} for wind speeds of 2 m s^{-1} to 3.5 m s^{-1}, 3.5 m s^{-1} to 5 m s^{-1}, 5 m s^{-1} to 6.5
560 m s^{-1}, 6.5 m s^{-1} to 8 m s^{-1}, and 8 m s^{-1} to 9.5 m s^{-1}, respectively.

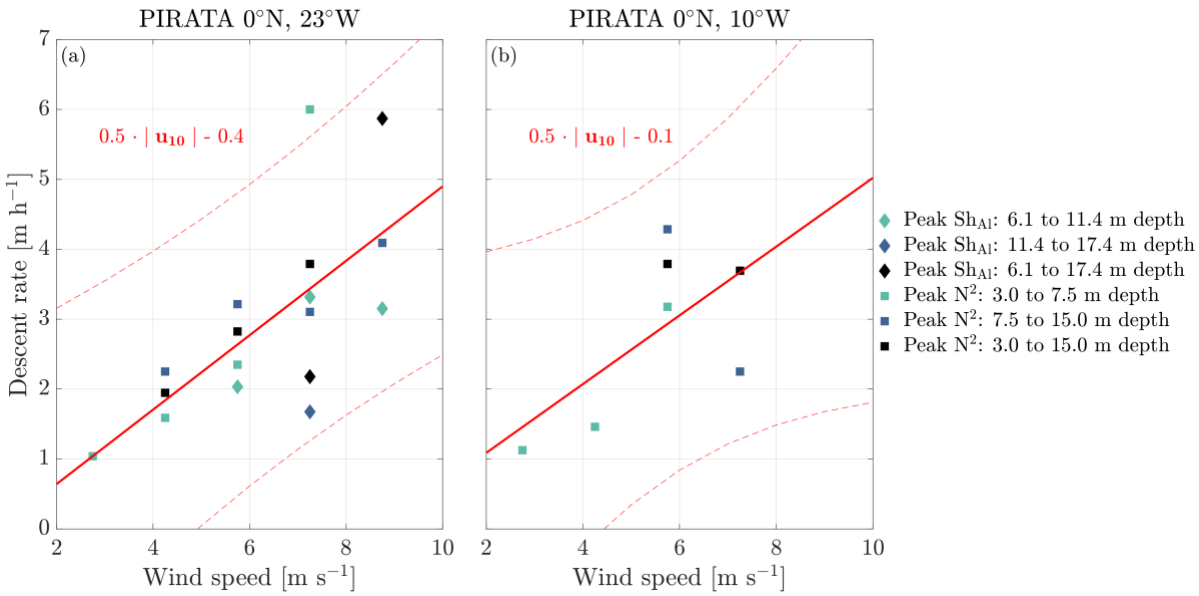

561

562 *Figure 8. Descent rates as a function of wind speed. The descent rates are calculated from the peaks of N^2 (square)*
563 *and Sh_{AI} (diamond) which are shown in Figures 6e and 7e for (a) the PIRATA site at 0°N, 23°W and (b) the PIRATA*
564 *site at 0°N, 10°W. The different depth intervals are indicated in colour. The red lines represent a linear fit to the*
565 *data (solid) and the associated 95% prediction interval (dashed).*

566 According to the timing of the peaks, descent rates of both diurnal Sh_{AI} and N^2 increase
567 with increasing wind speed (Figure 8a). There seems to be a linear relationship between the wind
568 speed and the descent rate: for every increase of 2 m s^{-1} in wind speed, the descent rate appears
569 to increase by 1 m h^{-1}. Note that this linear regression is computed excluding one Sh_{AI} peak as an
570 outlier. The timing and amplitude of the diurnal cycle of N^2 at the PIRATA buoy at 0°N, 10°W
571 (not shown) are similar to the ones at 0°N, 23°W presented before. The descent rates are also
572 similar, yielding the same slope of the linear fit for the descent rate as a function of the wind
573 speed (Figure 8b). The main differences between the mooring sites are a higher background

574 stratification at 30 m depth as well as enhanced variability at 15 m depth disguising the diurnal
575 signal at 10°W compared to 23°W.

576 **6 Summary and Discussion**

577 This study focusses on the diurnal cycles of shear and stratification, respectively called
578 the diurnal jet and the DWL, in the upper 20 m of the equatorial Atlantic and on their wind
579 dependence. Shear and stratification are primarily derived from drifter experiments and
580 shipboard measurements during the TRATLEQ expeditions in October 2019 and May 2022.
581 These two seasons differed in wind direction, net surface heat flux as well as strength and depth
582 of the EUC but were comparable in wind speed. Despite these partly contrasting conditions,
583 similar diurnal jets with an amplitude of about 11 cm s^{-1} and similar DWLs are observed. The
584 main difference between the expeditions is the 5 cm s^{-1} background velocity difference between
585 0.5 m and 15 m depth in May 2022, associated with a shallower and stronger EUC (Brandt et al.,
586 2023). We suggest that zonal background shear is mainly related to the vertical migration of the
587 EUC core (Brandt et al., 2016, 2023) and meridional background shear to the presence of the
588 equatorial roll (Heukamp et al., 2022), with zonal background shear being dominant. The
589 generalizability of this statement is limited as we only considered two points in time. Potential
590 constraints of the analysed velocity and associated shear estimates are the various vertical ranges
591 (drogue length of drifters, wave length of the dominant surface waves defining the penetration
592 depth of the marine radar, and bin size of the vmADCP), which are averaged to obtain the
593 assigned depth values, and wind slip for drifter measurements (see Text S1 for more details).
594 Still, the observed diurnal jets are in the range of previous observational results in the tropical
595 and subtropical Atlantic and Pacific (Price et al., 1986; Kudryavtsev & Soloviev, 1990; Cronin &
596 Kessler, 2009; Wenegrat & McPhaden, 2015; Sutherland et al., 2016), although a direct
597 comparison of diurnal jet diagnostics is complicated by the use of different depth levels and by
598 different background and in particular wind conditions. The comparison of the two TRATLEQ
599 expeditions suggests that, at least for wind speeds around 6 m s^{-1}, the diurnal jet amplitude is
600 independent of the surface heat flux and the wind direction but possibly dependent on the wind
601 speed. For lower wind speeds, it is possible that the surface heat flux plays a role again
602 (Matthews et al., 2014). The hypothesis of a wind speed dependence of the diurnal jet amplitude

603 is tested and supported by examining observational records with a larger spread in wind
604 conditions taken at the PIRATA buoys.
605
606 At the PIRATA buoy at 0°N, 23°W, diurnal jets and DWLs are observed for wind speeds
607 ranging from 2 m s^{-1} to 9.5 m s^{-1} and from 0.5 m s^{-1} to 9.5 m s^{-1}, respectively. Both diurnal jet
608 and DWL descend deeper and reach their peak earlier for stronger winds. For the DWL, the
609 diurnal stratification amplitude increases with decreasing wind speed. For the diurnal jet, the
610 diurnal shear amplitude at 6 m depth is maximum for moderate wind speeds of 5 m s^{-1} to 6.5 m s^{-1}.
611 At 11 m depth and below, the diurnal shear amplitude is maximum for maximum wind speeds.
612 In the following, we will discuss 1. wind speed thresholds, 2. wind speed dependence of the
613 penetration depth, and 3. wind speed dependence of diurnal amplitudes.

614 1. Our findings match with model results suggesting a minimum wind speed threshold of 2
615 m s^{-1} for the existence of a diurnal jet (Hughes et al., 2020a, 2021). However, our
616 observations do not support a maximum wind speed threshold (at least up to 9.5 m s^{-1}
617 winds) for both DWL and diurnal jet as found by Hughes et al. (2021) with 8 m s^{-1} in the
618 subtropical Pacific, by Thompson et al. (2019) with 7.6 m s^{-1} in the equatorial Indian
619 Ocean, by Matthews et al. (2014) with 6 m s^{-1} in the equatorial Indian Ocean, and by
620 Kudryavtsev & Soloviev (1990) with roughly 6.6 m s^{-1} in the equatorial Atlantic. In
621 contrast, our observations indicate even for wind speeds of 8 m s^{-1} to 9.5 m s^{-1} (no
622 observations for higher wind speeds) the presence of a weak but sufficient DWL to trap
623 wind momentum and to generate a diurnal jet. However, we do see a wind speed
624 threshold of about 6 m s^{-1} above which the daily-mean stratification is clearly reduced.
625 Followingly, the discrepancy between our findings and previous studies might be a result
626 of varying definitions of the DWL, especially with respect to thresholds such as
627 minimum penetration depth and minimum diurnal amplitude. The existence of diurnal
628 dynamics also for high wind speeds, as suggested in this study, indicates that also DCT
629 can occur in those wind conditions.
630 2. Our results indicate an increase in the penetration depth of the diurnal jet and the DWL
631 with increasing wind speed. This is in line with earlier observations (Price et al., 1986;
632 Hughes et al., 2020b; Masich et al., 2021). Note that our results give the impression that
633 the DWL reaches deeper than the diurnal jet. We assume that this is solely a consequence

of a reduced signal-to-noise ratio of the velocity data, leading to the signal of the descending diurnal jet being lost earlier than the one of the DWL. The maximum penetration depth for the DWL and the diurnal jet should be the same, as shown, e.g., in Smyth et al. (2013).

3. We find that a stronger wind stress does not necessarily generate stronger vertical shear between fixed depth levels in the upper ocean, a behaviour opposite to that of a classical wall layer, as Price et al. (1986) already observed. As a function of wind speed, we find small but noticeable variations in the diurnal jet amplitude between 0.5 m and 15 m depth and distinct variations considering smaller depth intervals. In contrast to our observations, a near-uniform diurnal jet amplitude has been previously suggested which only depends on the net surface heat flux and is independent of the wind stress (Price et al., 1986; Sutherland et al., 2016). An idealised simulation by Hughes et al. (2020a) showed a dependence of the maximum shear on the wind speed for all considered mixing schemes with the maximum shear decreasing with increasing wind speed for winds stronger than 2 m s^{-1}. A main difference between our observations and those used for previous studies is the duration with only a few days of measurements in the previous studies. Therefore, one possible explanation for the different conclusions on wind dependence might be the hypothesis of a memory of previous diurnal events (Sutherland et al., 2016). If a memory exists, changes in wind speed will have little influence on the diurnal diagnostics considering a time span of a few days but will be apparent in longer observational records. However, the observed decrease in the diurnal amplitude with depth for all wind speeds (except for the diurnal jet at winds of 8 m s^{-1} – 9.5 m s^{-1}) suggests that the amplitude of both the diurnal jet and DWL will be underestimated if a shallowest usable depth of 11 m (Masich et al., 2021) or 10 m (Smyth et al., 2013) is used. This stresses the importance of near-surface measurements to properly evaluate the near-surface heat and momentum budget.

6.1 Descent rates of diurnal jet and diurnal warm layer and their relation to deep-cycle turbulence as a function of wind speed

This study demonstrates the wind dependence of the timing of the diurnal peak for both shear and stratification. In line with observations by Smyth et al. (2013), the timing of the two

parameters is usually similar. We find at all considered depth levels earlier shear and stratification peaks for stronger winds, consistent with the simulation by Hughes et al. (2020a). Furthermore, we find that the descent rates of shear and stratification peaks increase with higher wind speed with values of 1.0 m h^{-1}, 1.9 m h^{-1}, 2.8 (2.0) m h^{-1}, 3.8 (2.2) m h^{-1}, and 4.1 (5.9) m h^{-1} for wind speeds of 2 m s^{-1} to 3.5 m s^{-1}, 3.5 m s^{-1} to 5 m s^{-1}, 5 m s^{-1} to 6.5 m s^{-1}, 6.5 m s^{-1} to 8 m s^{-1}, and 8 m s^{-1} to 9.5 m s^{-1} considering stratification (shear), respectively. According to a linear regression, the descent rate increases by 1 m h^{-1} every 2 m s^{-1} wind speed. The observed descent rates are in line with observations for the DWL descent by Hughes et al. (2020b) who found descent rates in the upper 8 m of the ocean of 0.3 m h^{-1}, 1 m h^{-1}, and 4 m h^{-1} for wind speeds of 1.6 m s^{-1}, 4.0 m s^{-1}, and 7.6 m s^{-1}, respectively. The observed descent rate of 2 m h^{-1} in the upper 20 m of the ocean for mean winds of 6 m s^{-1} by Sutherland et al. (2016) is also in agreement with our results. The fact that these two experiments were conducted away from the equator (12°N to 18°N and 25.6°N, respectively) and match our results suggests that the descent rate is independent of the Coriolis parameter at least up to subtropical regions. Furthermore, the 6 m h^{-1} descent rate for both the DWL and the diurnal jet observed by Smyth et al. (2013) in 15 m to 50 m depth in the equatorial Pacific for a mean wind speed at 10 m height of about 8 m s^{-1} is at the upper limit of the above-mentioned relations. The multi-monthly mean (May 2004 to February 2005) descent rate of the diurnal jet of 5 m h^{-1} observed between 7.5 m and 17.5 m depth also in the equatorial Pacific for mean winds at 10 m height of 7 m s^{-1} (Pham et al., 2017) also exceeds our observations. The higher descent rates observed in the equatorial Pacific compared to our findings in the equatorial Atlantic could indicate the presence of background conditions in the equatorial Pacific that facilitate the descent. We expect that marginal instability could be such a condition as it was found to be more present in the equatorial Pacific than Atlantic (Moum et al., 2023) and it is assumed to facilitate the descent of the diurnal jet (Lien et al., 1995; Masich et al., 2021). However, marginal instability has not been analysed in this study and further research is needed to identify the causalities of possible different descent rates in the equatorial Atlantic and Pacific.

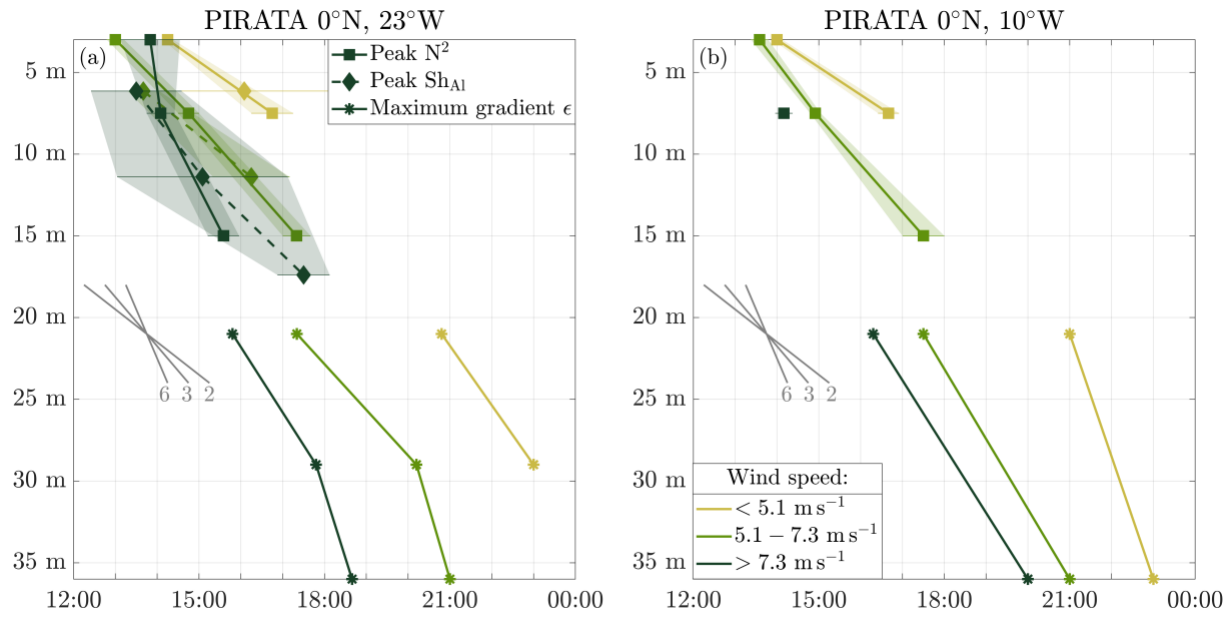

Figure 9. Descent of DWL, diurnal jet, and DCT as a function of SAT, depth and wind speed at the PIRATA sites (a) 0°N, 23°W and (b) 0°N, 10°W. N^2 peaks (square), Sh_{Al} peaks (diamond), and the times of maximum temporal dissipation (ε) gradient (asterisk, estimated from Figure 9 of Moum et al. (2023)) are presented for three different wind groups in colour. The shading marks the 95% CIs to estimate the fitted diurnal peak. As a reference for the descent rates, nominal slopes of 2 m h^{-1}, 3 m h^{-1} and 6 m h^{-1} are indicated by the grey lines.

The observed timing of the diurnal stratification and shear peaks as a function of depth and wind speed can be used to examine the hypothesis of Moum et al. (2023) that the wind-dependent delay of DCT may be a direct result of the wind-dependent DWL deepening. Both the maximum temporal dissipation gradient found by Moum et al. (2023) and the peak of stratification and shear at the PIRATA mooring sites (Figure 9) show an earlier onset or peak, repectively, for stronger winds. This indicates that the wind-dependent descent rates of the DWL and the diurnal jet indicated in this study also reflect in the timing of DCT. However, it remains unclear when and where instabilities are triggered. The exact timing of the onset and the peak of diurnal shear, shear instabilities and DCT might also depend on background stratification and shear. Further studies are needed to better understand the processes. We suggest that studying DCT as a function of wind speed can help to relate the wind-dependent diurnal jet to DCT, for which Moum et al. (2023) found a wind dependence of the strength but not of the descent rate. Note that also the wind-dependent strength of DCT might be explained by the wind-dependent penetration depth and amplitude of the diurnal jet.

6.2 Impact of the diurnal cycle on the wind power input

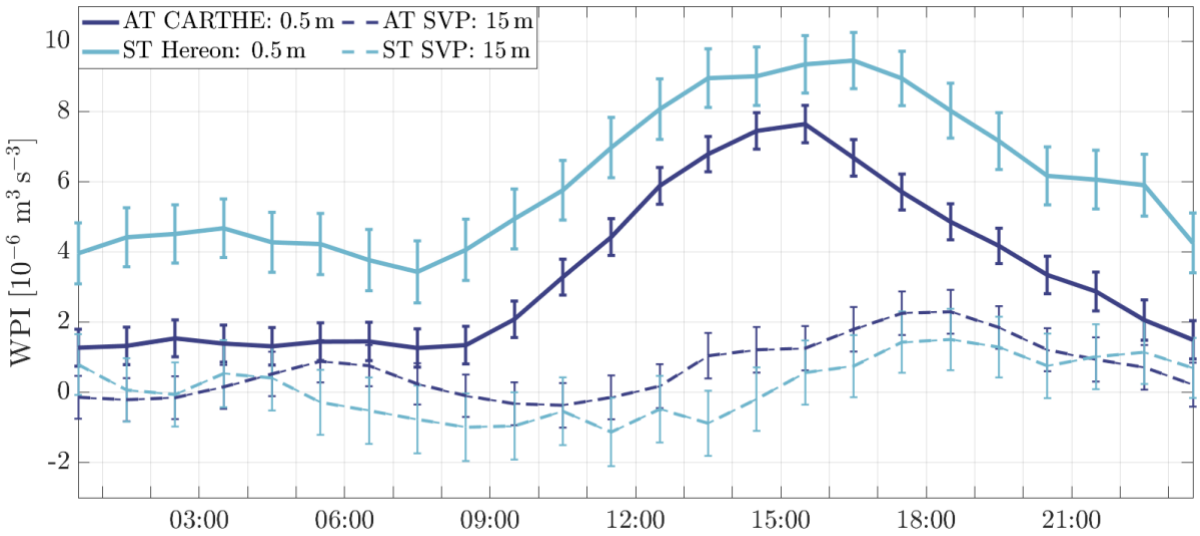

Figure 10. Mean diurnal cycles of WPI as a function of SAT. The WPI is computed for spring (ST, light blue) and autumn (AT, dark blue) TRATLEQ drifter experiments with velocities at 0.5 m and at 15 m depth depicted by solid and dashed lines, respectively. The error bars represent the standard error.

The near-surface diurnal dynamics described in this study also reflect in the WPI (Figure 10) and thus impact the amount of mechanical energy transferred by winds into the ocean. There is a diurnal cycle in the WPI derived from the autumn (spring) TRATLEQ drifter velocities at 0.5 m depth, leading to a 1.62 (1.60) $*10^{-6}$ $m^3 s^{-3}$, i.e., 59% (32%) increase of the diurnal mean WPI compared to the night-time WPI. The calculation of a fictive WPI using the autumn (spring) TRATLEQ drifter velocities at 15 m depth leads to a reduction of the WPI by 80% (96%). This underestimation of the available surface kinetic energy stresses the relevance of considering the diurnal jet and of actually observing surface velocities instead of taking, e.g., 15 m velocities as surface velocities. Furthermore, it shows that DWL and diurnal jet not only impact energy transfer into the mixed layer but also impact air-sea fluxes and the amount of energy within the DWL and below which is available for mixing.

7 Conclusion

This study examines the diurnal jet and DWL in the equatorial Atlantic, focussing on the impact of the wind speed. Our analysis demonstrates that the wind speed influences timing, amplitude, penetration depth, and descent rate of DWL and diurnal jet. The presented wind-

731 dependent descent rate of the diurnal jet and DWL can explain the wind-dependent onset of
732 DCT. Furthermore, the diurnal dynamics impact the energy input into the ocean through the
733 WPI. The question of how much of this energy is used to enhance turbulence during the descent
734 of the DWL in the DCT layer remains open. Our results enhance the understanding of diurnal
735 dynamics and stress the importance of near-surface measurements of, in particular, velocity. We
736 want to emphasize that satellite missions aiming to resolve absolute ocean currents could provide
737 additional data for better regional characterization of diurnal surface velocity variability
738 (Ardhuin et al., 2019; Villas Bôas et al., 2019). Our results and in particular the TRATLEQ
739 velocity data sets, which allow for a basin-scale view of velocities and shear in the upper metres
740 of the ocean and which are presented in this study for the first time, can contribute to calibrate
741 and validate satellite missions that aim to resolve absolute ocean currents like the current SWOT
742 mission (Morrow et al., 2019) or possible future missions based on advanced Doppler-radar
743 techniques as suggested for Odysea (Rodríguez et al., 2019) or SKIM (Ardhuin et al., 2018). Our
744 results will enable the examination of possible offsets of satellite measurements due to sampling
745 at various hours of the day. This study can also facilitate the validation of ocean models that aim
746 to resolve diurnal dynamics (Bernie et al., 2007), aim to be energetically consistent (Eden et al.,
747 2014; Gutjahr et al., 2021), or aim to correctly represent surface currents for other applications,
748 e.g., to deduce Sargassum drift (Van Sebille et al., 2021). Moreover, this study points out that the
749 diurnal cycle can be captured by vessel-mounted observation systems, which might be useful for
750 further studies on spatial pattern of diurnal dynamics.

751 **Acknowledgments**

752 This study was supported by the EU H2020 under grant agreement 817578 TRIATLAS project.
753 F. Gasparin and S. Cravatte are funded by IRD, Institut de Recherche pour le Développement
754 (the French National Research Institute for Sustainable Development). G. Reverdin is funded by
755 CNRS (the French Centre National de la recherche scientifique). Part of this work was carried
756 out during a scientific visit of A.C. Hans at LEGOS, funded by the TOSCA/CNES STREAM
757 project and the LEFE/GMMC PODIOM project. The authors thank the captains and crews of RV
758 Meteor, as well as scientists and technicians who contributed to collecting the observational data
759 used in this study during the TRATLEQ cruises. The authors also thank Ruben Carrasco for
760 processing the marine radar measurements and Rena Czeschel for processing the vmADCP

measurements during autumn TRATLEQ. The authors are grateful to Fabrice Ardhuin for providing CARTHE drifters. SVP drifters were freely provided by different institutions for deployment in the equatorial Atlantic. The authors also acknowledge the GTMBA Project Office of NOAA/PMEL and the PIRATA programme for freely providing data from the tropical Atlantic buoy array. In particular, the authors thank Mike McPhaden for providing the EMP velocity data at the PIRATA buoy at 0°N, 23°W. The authors acknowledge that CCMP Version-2.0 analyses are produced by Remote Sensing Systems and sponsored by NASA Earth Science funding. The authors thank James N. Moum for helpful discussions.

Open Research

The marine radar and vmADCP measurements used to derive 3 m and 17 m depth on-track ocean velocities during autumn TRATLEQ are available at Pangaea in Carrasco & Horstmann (2024) and in Brandt et al. (2022), respectively. The drifter data used to derive velocities at 0.5 m and 15 m depth for autumn TRATLEQ in the study are available at Pangaea in Hans & Brandt (2021). For spring TRATLEQ, the Hereon drifter positions are available at Pangaea in Horstmann et al. (2023) and the SVP drifter positions at NOAA's OSMC ERDDAP via https://www.aoml.noaa.gov/phod/gdp/data.php with the relevant ID/WMO numbers listed in Table S2. The ID/WMO numbers of the SVP drifters deployed during autumn TRATLEQ are listed in Table S1. TSG, pitch and roll data to derive a stratification estimate at 4 m depth as well as wind and radiation data for the two TRATLEQ cruises are available at the Dship system via dship.bsh.de. Temperature, salinity and wind data from the PIRATA buoys used in this study are available from the Global Tropical Moored Buoy Array at https://www.pmel.noaa.gov/tao/drupal/disdel/. The access to the heat flux data used from ePIRATA is described at https://www.aoml.noaa.gov/phod/epirata/. The velocity data at the PIRATA site at 0°N, 23°W during the EMP are available at https://www.pmel.noaa.gov/tao/drupal/disdel/adcp_0n23w/index.html. The satellite CCMP V2.0 wind data are available at REMSS via www.remss.com (Wentz et al., 2015). All analyses were performed and all figures created using MATLAB R2021a.

References

Ardhuin, F., Aksenov, Y., Benetazzo, A., Bertino, L., Brandt, P., Caubet, E., et al. (2018).

Measuring currents, ice drift, and waves from space: the Sea surface KInematics Multiscale monitoring (SKIM) concept. *Ocean Science*, *14*(3), 337–354. https://doi.org/10.5194/os-14-337-2018

Ardhuin, F., Brandt, P., Gaultier, L., Donlon, C., Battaglia, A., Boy, F., et al. (2019). SKIM, a Candidate Satellite Mission Exploring Global Ocean Currents and Waves. *Frontiers in Marine Science*, *6*, 209. https://doi.org/10.3389/fmars.2019.00209

Bellenger, H., & Duvel, J.-P. (2009). An Analysis of Tropical Ocean Diurnal Warm Layers. *Journal of Climate*, *22*(13), 3629–3646. https://doi.org/10.1175/2008JCLI2598.1

Bernie, D. J., Guilyardi, E., Madec, G., Slingo, J. M., & Woolnough, S. J. (2007). Impact of resolving the diurnal cycle in an ocean–atmosphere GCM. Part 1: a diurnally forced OGCM. *Climate Dynamics*, *29*(6), 575–590. https://doi.org/10.1007/s00382-007-0249-6

Bourlès, B., Araujo, M., McPhaden, M. J., Brandt, P., Foltz, G. R., Lumpkin, R., et al. (2019). PIRATA: A Sustained Observing System for Tropical Atlantic Climate Research and Forecasting. *Earth and Space Science*, *6*(4), 577–616. https://doi.org/10.1029/2018EA000428

Brandt, P., Claus, M., Greatbatch, R. J., Kopte, R., Toole, J. M., Johns, W. E., & Böning, C. W. (2016). Annual and Semiannual Cycle of Equatorial Atlantic Circulation Associated with Basin-Mode Resonance. *Journal of Physical Oceanography*, *46*(10), 3011–3029. https://doi.org/10.1175/JPO-D-15-0248.1

Brandt, P., Czeschel, R., & Krahmann, G. (2022). ADCP current measurements (38 and 75 kHz) during METEOR cruise M158 [Data set]. https://doi.org/10.1594/PANGAEA.952101

Brandt, P., Alory, G., Awo, F. M., Dengler, M., Djakouré, S., Imbol Koungue, R. A., et al. (2023). Physical processes and biological productivity in the upwelling regions of the

tropical Atlantic. *Ocean Science*, *19*(3), 581–601. https://doi.org/10.5194/os-19-581-2023

Carrasco, R., & Horstmann, J. (2024). Radar-Derived Surface Current Fields Along Meteor Cruise M158 [Data set]. to be submitted.

Cronin, M. F., & Kessler, W. S. (2009). Near-Surface Shear Flow in the Tropical Pacific Cold Tongue Front*. *Journal of Physical Oceanography*, *39*(5), 1200–1215. https://doi.org/10.1175/2008JPO4064.1

Dutton, J. A. (1995). *Dynamics of atmospheric motion* (Unabridged and unaltered reproduction). New York, NY: Dover Publications.

Eden, C., Czeschel, L., & Olbers, D. (2014). Toward Energetically Consistent Ocean Models. *Journal of Physical Oceanography*, *44*(12), 3160–3184. https://doi.org/10.1175/JPO-D-13-0260.1

Efron, B. (1979). Bootstrap Methods: Another Look at the Jackknife. *The Annals of Statistics*, *7*(1). https://doi.org/10.1214/aos/1176344552

Elipot, S., & Wenegrat, J. O. (2021). Vertical Structure of near-surface currents - Importance, state of knowledge, and measurement challenges. *US CLIVAR VARIATIONS*, *19*(1). https://doi.org/10.5065/YBCA-0S03

Fischer, J., Brandt, P., Dengler, M., Müller, M., & Symonds, D. (2003). Surveying the Upper Ocean with the Ocean Surveyor: A New Phased Array Doppler Current Profiler. *Journal of Atmospheric and Oceanic Technology*, *20*(5), 742–751. https://doi.org/10.1175/1520-0426(2003)20<742:STUOWT>2.0.CO;2

Fischer, T., Kock, A., Arévalo-Martínez, D. L., Dengler, M., Brandt, P., & Bange, H. W. (2019). Gas exchange estimates in the Peruvian upwelling regime biased by multi-day near-surface stratification. *Biogeosciences*, *16*(11), 2307–2328. https://doi.org/10.5194/bg-16-

2307-2019

Fleagle, R. G., & Businger, J. A. (1980). *An introduction to atmospheric physics* (2d ed). New York: Academic Press.

Foltz, G. R., Schmid, C., & Lumpkin, R. (2018). An Enhanced PIRATA Dataset for Tropical Atlantic Ocean–Atmosphere Research. *Journal of Climate*, *31*(4), 1499–1524. https://doi.org/10.1175/JCLI-D-16-0816.1

Gutjahr, O., Brüggemann, N., Haak, H., Jungclaus, J. H., Putrasahan, D. A., Lohmann, K., & Von Storch, J.-S. (2021). Comparison of ocean vertical mixing schemes in the Max Planck Institute Earth System Model (MPI-ESM1.2). *Geoscientific Model Development*, *14*(5), 2317–2349. https://doi.org/10.5194/gmd-14-2317-2021

Hans, A. C., & Brandt, P. (2021). Surface drifter data from Meteor cruise M158 [Data set]. https://doi.org/10.1594/PANGAEA.926752

Heukamp, F. O., Brandt, P., Dengler, M., Tuchen, F. P., McPhaden, M. J., & Moum, J. N. (2022). Tropical Instability Waves and Wind-Forced Cross-Equatorial Flow in the Central Atlantic Ocean. *Geophysical Research Letters*, *49*(19), e2022GL099325. https://doi.org/10.1029/2022GL099325

Horstmann, J., Borge, J. C. N., Seemann, J., Carrasco, R., & Lund, B. (2015). Wind, Wave, and Current Retrieval Utilizing X-Band Marine Radars. In *Coastal Ocean Observing Systems* (pp. 281–304). Elsevier. https://doi.org/10.1016/B978-0-12-802022-7.00016-X

Horstmann, J., Bödewadt, J., Carrasco, R., Cysewski, M., Seemann, J., & Streβer, M. (2021). A Coherent on Receive X-Band Marine Radar for Ocean Observations. *Sensors*, *21*(23), 7828. https://doi.org/10.3390/s21237828

Horstmann, J., Navarro, W., Carrasco, R., Brandt, P., Hans, A. C., & Prigent, A. (2023). Surface

Drifter Data of the Equatorial Atlantic: Positions of Lagrangian Hereon Drifters deployed in the Equatorial Atlantic during METEOR Cruise M181 [Data set]. https://doi.org/10.1594/PANGAEA.955925

Hughes, K. G., Moum, J. N., & Shroyer, E. L. (2020a). Evolution of the Velocity Structure in the Diurnal Warm Layer. *Journal of Physical Oceanography*, *50*(3), 615–631. https://doi.org/10.1175/JPO-D-19-0207.1

Hughes, K. G., Moum, J. N., & Shroyer, E. L. (2020b). Heat Transport through Diurnal Warm Layers. *Journal of Physical Oceanography*, *50*(10), 2885–2905. https://doi.org/10.1175/JPO-D-20-0079.1

Hughes, K. G., Moum, J. N., Shroyer, E. L., & Smyth, W. D. (2021). Stratified shear instabilities in diurnal warm layers. *Journal of Physical Oceanography*. https://doi.org/10.1175/JPO-D-20-0300.1

IOC / SCOR / IAPSO. (2010). The international thermodynamic equation of seawater - 2010: Calculation and use of thermodynamic properties. Intergovernmental Oceanographic Commission, Manuals and Guides, No. 56.

Koblick, D. (2021). Convert UTC to Solar Apparent Time. Retrieved from https://www.mathworks.com/matlabcentral/fileexchange/32804-convert-utc-to-solar-apparent-time

Kudryavtsev, V. N., & Soloviev, A. V. (1990). Slippery Near-Surface Layer of the Ocean Arising Due to Daytime Solar Heating. *Journal of Physical Oceanography*, *20*(5), 617–628. https://doi.org/10.1175/1520-0485(1990)020<0617:SNSLOT>2.0.CO;2

Lien, R. -C., Caldwell, D. R., Gregg, M. C., & Moum, J. N. (1995). Turbulence variability at the equator in the central Pacific at the beginning of the 1991–1993 El Niño. *Journal of*

884 *Geophysical Research: Oceans*, *100*(C4), 6881–6898. https://doi.org/10.1029/94JC03312
885 Lund, B., Haus, B. K., Horstmann, J., Graber, H. C., Carrasco, R., Laxague, N. J. M., et al.
886 (2018). Near-Surface Current Mapping by Shipboard Marine X-Band Radar: A
887 Validation. *Journal of Atmospheric and Oceanic Technology*, *35*(5), 1077–1090.
888 https://doi.org/10.1175/JTECH-D-17-0154.1
889 Masich, J., Kessler, W. S., Cronin, M. F., & Grissom, K. R. (2021). Diurnal Cycles of Near-
890 Surface Currents Across the Tropical Pacific. *Journal of Geophysical Research: Oceans*,
891 *126*(4), e2020JC016982. https://doi.org/10.1029/2020JC016982
892 Matthews, A. J., Baranowski, D. B., Heywood, K. J., Flatau, P. J., & Schmidtko, S. (2014). The
893 Surface Diurnal Warm Layer in the Indian Ocean during CINDY/DYNAMO. *Journal of*
894 *Climate*, *27*(24), 9101–9122. https://doi.org/10.1175/JCLI-D-14-00222.1
895 Morrow, R., Fu, L.-L., Ardhuin, F., Benkiran, M., Chapron, B., Cosme, E., et al. (2019). Global
896 Observations of Fine-Scale Ocean Surface Topography With the Surface Water and
897 Ocean Topography (SWOT) Mission. *Frontiers in Marine Science*, *6*, 232.
898 https://doi.org/10.3389/fmars.2019.00232
899 Moum, J. N., & Caldwell, D. R. (1985). Local Influences on Shear-Flow Turbulence in the
900 Equatorial Ocean. *Science*, *230*(4723), 315–316.
901 https://doi.org/10.1126/science.230.4723.315
902 Moum, J. N., Perlin, A., Nash, J. D., & McPhaden, M. J. (2013). Seasonal sea surface cooling in
903 the equatorial Pacific cold tongue controlled by ocean mixing. *Nature*, *500*(7460), 64–67.
904 https://doi.org/10.1038/nature12363
905 Moum, J. N., Hughes, K. G., Shroyer, E. L., Smyth, W. D., Cherian, D., Warner, S. J., et al.
906 (2022). Deep Cycle Turbulence in Atlantic and Pacific Cold Tongues. *Geophysical*

Research Letters, *49*(8), e2021GL097345. https://doi.org/10.1029/2021GL097345

Moum, J. N., Smyth, W. D., Hughes, K. G., Cherian, D., Warner, S. J., Bourlès, B., et al. (2023). Wind Dependencies of Deep Cycle Turbulence in the Equatorial Cold Tongues. *Journal of Physical Oceanography*, *53*(8), 1979–1995. https://doi.org/10.1175/JPO-D-22-0203.1

Pacanowski, R. C. (1987). Effect of Equatorial Currents on Surface Stress. *Journal of Physical Oceanography*, *17*(6), 833–838. https://doi.org/10.1175/1520-0485(1987)017<0833:EOECOS>2.0.CO;2

Peters, H., Gregg, M. C., & Toole, J. M. (1988). On the parameterization of equatorial turbulence. *Journal of Geophysical Research: Oceans*, *93*(C2), 1199–1218. https://doi.org/10.1029/JC093iC02p01199

Pham, H. T., Sarkar, S., & Winters, K. B. (2013). Large-Eddy Simulation of Deep-Cycle Turbulence in an Equatorial Undercurrent Model. *Journal of Physical Oceanography*, *43*(11), 2490–2502. https://doi.org/10.1175/JPO-D-13-016.1

Pham, H. T., Smyth, W. D., Sarkar, S., & Moum, J. N. (2017). Seasonality of Deep Cycle Turbulence in the Eastern Equatorial Pacific. *Journal of Physical Oceanography*, *47*(9), 2189–2209. https://doi.org/10.1175/JPO-D-17-0008.1

Price, J. F., Weller, R. A., & Pinkel, R. (1986). Diurnal cycling: Observations and models of the upper ocean response to diurnal heating, cooling, and wind mixing. *Journal of Geophysical Research: Oceans*, *91*(C7), 8411–8427. https://doi.org/10.1029/JC091iC07p08411

Radenac, M.-H., Jouanno, J., Tchamabi, C. C., Awo, M., Bourlès, B., Arnault, S., & Aumont, O. (2020). Physical drivers of the nitrate seasonal variability in the Atlantic cold tongue. *Biogeosciences*, *17*(2), 529–545. https://doi.org/10.5194/bg-17-529-2020

Rodríguez, E., Bourassa, M., Chelton, D., Farrar, J. T., Long, D., Perkovic-Martin, D., & Samelson, R. (2019). The Winds and Currents Mission Concept. *Frontiers in Marine Science*, *6*, 438. https://doi.org/10.3389/fmars.2019.00438

Röhrs, J., Sutherland, G., Jeans, G., Bedington, M., Sperrevik, A. K., Dagestad, K.-F., et al. (2021). Surface currents in operational oceanography: Key applications, mechanisms, and methods. *Journal of Operational Oceanography*, *16*(1), 60–88. https://doi.org/10.1080/1755876X.2021.1903221

Smyth, W. D., & Moum, J. N. (2013). Marginal instability and deep cycle turbulence in the eastern equatorial Pacific Ocean. *Geophysical Research Letters*, *40*(23), 6181–6185. https://doi.org/10.1002/2013GL058403

Smyth, W. D., Moum, J. N., Li, L., & Thorpe, S. A. (2013). Diurnal Shear Instability, the Descent of the Surface Shear Layer, and the Deep Cycle of Equatorial Turbulence. *Journal of Physical Oceanography*, *43*(11), 2432–2455. https://doi.org/10.1175/JPO-D-13-089.1

Smyth, W. D., Nash, J. D., & Moum, J. N. (2019). Self-organized criticality in geophysical turbulence. *Scientific Reports*, *9*(1), 3747. https://doi.org/10.1038/s41598-019-39869-w

St. Laurent, L., & Merrifield, S. (2017). Measurements of Near-Surface Turbulence and Mixing from Autonomous Ocean Gliders. *Oceanography*, *30*(2), 116–125. https://doi.org/10.5670/oceanog.2017.231

Sutherland, G., Marié, L., Reverdin, G., Christensen, K. H., Broström, G., & Ward, B. (2016). Enhanced Turbulence Associated with the Diurnal Jet in the Ocean Surface Boundary Layer. *Journal of Physical Oceanography*, *46*(10), 3051–3067. https://doi.org/10.1175/JPO-D-15-0172.1

Thompson, E. J., Moum, J. N., Fairall, C. W., & Rutledge, S. A. (2019). Wind Limits on Rain Layers and Diurnal Warm Layers. *Journal of Geophysical Research: Oceans*, *124*(2), 897–924. https://doi.org/10.1029/2018JC014130

Van Sebille, E., Zettler, E., Wienders, N., Amaral-Zettler, L., Elipot, S., & Lumpkin, R. (2021). Dispersion of Surface Drifters in the Tropical Atlantic. *Frontiers in Marine Science*, *7*, 607426. https://doi.org/10.3389/fmars.2020.607426

Villas Bôas, A. B., Ardhuin, F., Ayet, A., Bourassa, M. A., Brandt, P., Chapron, B., et al. (2019). Integrated Observations of Global Surface Winds, Currents, and Waves: Requirements and Challenges for the Next Decade. *Frontiers in Marine Science*, *6*, 425. https://doi.org/10.3389/fmars.2019.00425

Waliser, D. E., & Gautier, C. (1993). A Satellite-derived Climatology of the ITCZ. *Journal of Climate*, *6*(11), 2162–2174. https://doi.org/10.1175/1520-0442(1993)006<2162:ASDCOT>2.0.CO;2

Wenegrat, J. O., & McPhaden, M. J. (2015). Dynamics of the surface layer diurnal cycle in the equatorial Atlantic Ocean (0°, 23°W). *Journal of Geophysical Research: Oceans*, *120*(1), 563–581. https://doi.org/10.1002/2014JC010504

Wenegrat, J. O., McPhaden, M. J., & Lien, R. (2014). Wind stress and near-surface shear in the equatorial Atlantic Ocean. *Geophysical Research Letters*, *41*(4), 1226–1231. https://doi.org/10.1002/2013GL059149

Wentz, F. J., Scott, J., Hoffmann, R., Leidner, M., & Atlas, R. (2015). Remote Sensing Systems Cross-Calibrated Multi-Platform (CCMP) 6-hourly ocean vector wind analysis product on 0.25 deg grid, Version 2.0. [Data set]. Remote Sensing Systems, Santa Rosa, CA.

Whitt, D. B., Cherian, D. A., Holmes, R. M., Bachman, S. D., Lien, R.-C., Large, W. G., &

Moum, J. N. (2022). Simulation and Scaling of the Turbulent Vertical Heat Transport and Deep-Cycle Turbulence across the Equatorial Pacific Cold Tongue. *Journal of Physical Oceanography*, *52*(5), 981–1014. https://doi.org/10.1175/JPO-D-21-0153.1

Woods, J. D., & Strass, V. (1986). The response of the upper ocean to solar heating II: The wind-driven current. *Quarterly Journal of the Royal Meteorological Society*, *112*(471), 29–42. https://doi.org/10.1002/qj.49711247103

References From the Supporting Information

Haza, A. C., D'Asaro, E., Chang, H., Chen, S., Curcic, M., Guigand, C., et al. (2018). Drogue-Loss Detection for Surface Drifters during the Lagrangian Submesoscale Experiment (LASER). *Journal of Atmospheric and Oceanic Technology*, *35*(4), 705–725. https://doi.org/10.1175/JTECH-D-17-0143.1

Horstmann, J., Navarro, W., Carrasco, R., Brandt, P., Hans, A. C., & Prigent, A. (2023). Surface Drifter Data of the Equatorial Atlantic: Positions of Lagrangian Hereon Drifters deployed in the Equatorial Atlantic during METEOR Cruise M181 [Data set]. https://doi.org/10.1594/PANGAEA.955925

Lodise, J., Özgökmen, T., Griffa, A., & Berta, M. (2019). Vertical structure of ocean surface currents under high winds from massive arrays of drifters. *Ocean Science*, *15*(6), 1627–1651. https://doi.org/10.5194/os-15-1627-2019

Lumpkin, R., & Pazos, M. (2007). Measuring surface currents with Surface Velocity Program drifters: the instrument, its data, and some recent results. In A. Griffa, A. D. Kirwan, Jr., A. J. Mariano, T. Özgökmen, & H. T. Rossby (Eds.), *Lagrangian Analysis and Prediction of Coastal and Ocean Dynamics* (1st ed., pp. 39–67). Cambridge University Press. https://doi.org/10.1017/CBO9780511535901.003

1000 Niiler, P. P., Sybrandy, A. S., Bi, K., Poulain, P. M., & Bitterman, D. (1995). Measurements of
1001 the water-following capability of holey-sock and TRISTAR drifters. *Deep Sea Research*
1002 *Part I: Oceanographic Research Papers*, *42*(11–12), 1951–1964.
1003 https://doi.org/10.1016/0967-0637(95)00076-3
1004 Novelli, G., Guigand, C. M., Cousin, C., Ryan, E. H., Laxague, N. J. M., Dai, H., et al. (2017). A
1005 Biodegradable Surface Drifter for Ocean Sampling on a Massive Scale. *Journal of*
1006 *Atmospheric and Oceanic Technology*, *34*(11), 2509–2532.
1007 https://doi.org/10.1175/JTECH-D-17-0055.1
1008 Poulain, P.-M., Centurioni, L., & Özgökmen, T. (2022). Comparing the Currents Measured by
1009 CARTHE, CODE and SVP Drifters as a Function of Wind and Wave Conditions in the
1010 Southwestern Mediterranean Sea. *Sensors*, *22*(1), 353. https://doi.org/10.3390/s22010353
1011